Project Number: CF-FS17

DEVELOPMENT OF A POST-FABRICATION STIFFNESS CHARACTERIZATION TOOL FOR MEMS

A Major Qualifying Project Report
Submitted to the Faculty of the
WORCESTER POLYTECHNIC INSTITUTE
In partial fulfillment of the requirements for the
Degrees of Bachelor of Science in
Mechanical Engineering, Robotics Engineering, and Electrical Engineering
By

_____
Michael McConnell

_____
John Williams

_____
Shao Zhou

Date: 27 April 2017

Keywords:

1. MEMS Testing
2. Interferometry
3. Testing Automation

_____
Professor Cosme Furlong

Abstract

Micro-Electromechanical Systems (MEMS) manufacturers face difficulties in characterizing material properties of MEMS post production. Properties such as stiffness can be obtained from simultaneous force and displacement measurements in full-field. However, few automated quantitative tools that operate in the small workspace of high magnification imaging devices needed for such measurements exist. We developed a prototype MEMS metrology system that uses a sub-micro Newton resolution force probe operating under a nanometer resolution interferometer to characterize MEMS mechanical properties. FEA simulations and analytical calculations were performed to help determine system constraints and validate results. Precision actuators were integrated and controlled from a developed graphical user interface. The system was tested on an Analog Devices ADXL202 accelerometer.

Acknowledgements

This project was possible thanks to the equipment and lab space provided by the Center for Holographic Studies and Laser μmechaTronics (CHSLT) lab at WPI. We would like to extend our sincerest gratitude to the graduate students of the CHSLT lab. Their shared knowledge was critical in allowing the team to acquire needed materials and learn the required background information for this project. Payam Razavi, Haimi Tang, and Koohyar Pooladvand were particularly helpful. Additionally, the Opto-electronics Specialist and WPI Lab Monitor Peter Hefti provided the team with helpful filter analysis advice and electrical equipment.

The team also thanks WPI undergraduate student Domenic Bozzuto for allowing extensive usage of his personal 3d printer. This allowed the team to quickly develop many iterations of the metrology tool prototype's mounting brackets and the force probe cover.

Above all, the team would like to thank our project adviser Professor Cosme Furlong. His guidance in determining the project goals and scope were critical to maintaining the project's feasibility. He also provided the team with helpful feedback on design ideas and implementations.

Finally, the team thanks the Mechanical Engineering, Robotics Engineering, and Electrical Engineering Departments at Worcester Polytechnic Institute for providing the team with the necessary funds and education to make this project a success. It has been a challenging and rewarding experience.

Authorship

All team members contributed equally to this project.

Table of Contents

Table of Figures

List of Tables

Objectives

The goal of this project was to develop a metrology tool based on force and displacement measurements for *in situ* characterization of the physical properties of Micro-Electro-Mechanical Systems (MEMS). To accomplish this goal the team had the following objectives.

1. Develop a testing method for evaluating MEMS material properties
2. Design a metrology tool for simultaneous force and displacement sensing
3. Test the tool on an Analog Devices ADXL202 accelerometer

Executive Summary

Micro-Electromechanical Systems (MEMS) combine μm scale mechanical and electrical components. MEMS are manufactured using lithographic processes, which produce thousands of MEMS on individual polysilicon wafers, but variations in the production conditions usually lead to a mix of good and malfunctioning devices on the same wafer. Since packaging and testing of each die is up to 80% of the production costs, manufacturing costs can be reduced if MEMS are tested *in situ* prior to the packaging stage. The developed metrology tool prototype described in this paper conducts out of plane force and displacement testing on MEMS devices allowing for the extraction of material properties such as stiffness and elastic modulus.

To allow for full field displacement measurements, the developed prototype operates under a Michelson's Interferometer. An Interferometer is an optical device which uses the interference pattern of combined light beams to measure deformation at the nm scale. To measure forces, the system utilizes a FemtoTools FT-S1000-LAT force probe. This probe is a novel force sensor that has a resolution of 0.50 μN, allowing for precise force measurements that are previously difficult to conduct. To contact the device under test (DUT) using the force probe a series of precise actuators are used.

To position the DUT under the force probe, Newport TS-Series Linear stages are used. These stages have a resolution of 0.50 μm. The position of the DUT after movement using these stages is checked using a computer vision technique called Template Matching. This allows for precise planar positioning of the DUT.

To probe the DUT a two-stage process is employed. A National Aperture MM-3M-F.1 Linear Stage with a resolution of 0.12 μm was used to bring the force probe within 20 μm of the

DUT. Once this was done, final contact is made using a Thorlabs PAZ 005 Piezo Actuator. This actuator has the impressive resolution of 5 nm. This allowed for contact with the DUT to be done in a controlled and repeatable manner.

The entire system was controlled using a software package and Graphical User Interface (GUI) developed by the team. The GUI was written with Java, but the bulk of the software was written in MATLAB. This allowed the team to take advantage of MATLAB's easy to use Data Acquisition, Image Acquisition, and Image Processing toolboxes.

The MEMS device selected for testing was an ADXL202 Accelerometer. This is a 2-axis accelerometer common in car airbag deployment systems. In accordance with the Analytical, Computational, and Experimental Solutions (ACES) Methodology, the team performed analytical calculations and finite element analysis of the ADXL202 to develop expectations of the ADXL202 equivalent stiffness. The team utilized a previously developed equation for the out of plane displacement of a folded spring to produce an expected equivalent stiffness of 22 μN/μm. The team performed a Finite Element Analysis (FEA) on a 3D model of the ADXL202 using the software program ANSYS. This resulted in an alternative stiffness of 8.2 μN/μm. The disagreement between this value and the analytical calculations may be due to differences in ANSYS's calculated model mass and the one used for the previous calculations. Another explanation is that the analytical calculations do not account for deformations within the accelerometer proof mass. Interestingly, the experimental results of the team's tests on the ADXL202 using the force probe give an equivalent stiffness of 13 μN/μm a value which is between the previous expectations. Fortunately, the results obtained demonstrate that the prototype works as intended, and that the many components of the system have been successfully integrated. In the future, the interferometer should be used to analyze the

displacement on the DUT in more detail, which will help determine the source of variations between the results and expectations. Additionally, the system can be scaled up to operate on an entire wafer of MEMS devices to perform device performance testing prior to packaging.

1.0 Introduction

Modern technological systems grow increasingly complex with the continual development of new technologies. Yet, there is a constant demand from consumers to reduce the size of such systems. This can be seen most prominently in the consumer electronics sphere. For example, the iPhone 6 from Apple-Inc contains no less than 6 unique sensors and, still, easily fits inside an average pocket [1]. To meet this demand, many sensing and actuation systems have moved to micro or even nanometer scales. This is the realm of micro-electromechanical systems (MEMS). These systems use micrometer scale mechanisms, often manufactured on silicon, to either sense or induce electrical signals. Besides size reduction, MEMS devices also exhibit many other positive traits, such as high reliability, low power consumption and low cost to manufacture. As such, the MEMS industry has been growing rapidly in the past 40 years [2].

A common example of a MEMS device is a MEMS accelerometer (MEMSA). Originally used by the automotive industry for air bag deployment, MEMS accelerometers have now expanded into a range of other industries, and have an increasingly important role in navigation [2]. The number of MEMS accelerometers sold each year has increased from around 400 million in 2008 to almost 1.8 billion in 2014 [3]. In the inertial MEMS sensors market, accelerometers and gyroscopes contribute to a combined 20% of market sales [2]. With the rapid proliferation of accelerometer and gyroscope equipped smartphones and mechatronic systems, demand for MEMS accelerometers will likely continue to grow in the near future.

Though the capabilities of MEMS devices have advanced substantially in the past decades, there is still room for improvement. For example, high precision accelerometers requires costly calibration and testing to correct for subtle imperfections in output [4], [5].

Material properties at micrometer scales are still an area of intense research, and sources of error are not always predicted properly [6]. These inconsistencies from the MEMS manufacturing processes leads to poor yields which when coupled with high testing costs results in a major loss of revenue for the manufacturer.

MEMS are generally manufactured using the same lithographic processes as integrated circuits. Thousands of individual devices, known as dies, are produced on polysilicon wafers. These wafers are generally a standard size of 100, 200, or 300mm diameters. An example of a 200mm wafer of ADXL202 Accelerometers can be seen in Figure 1.

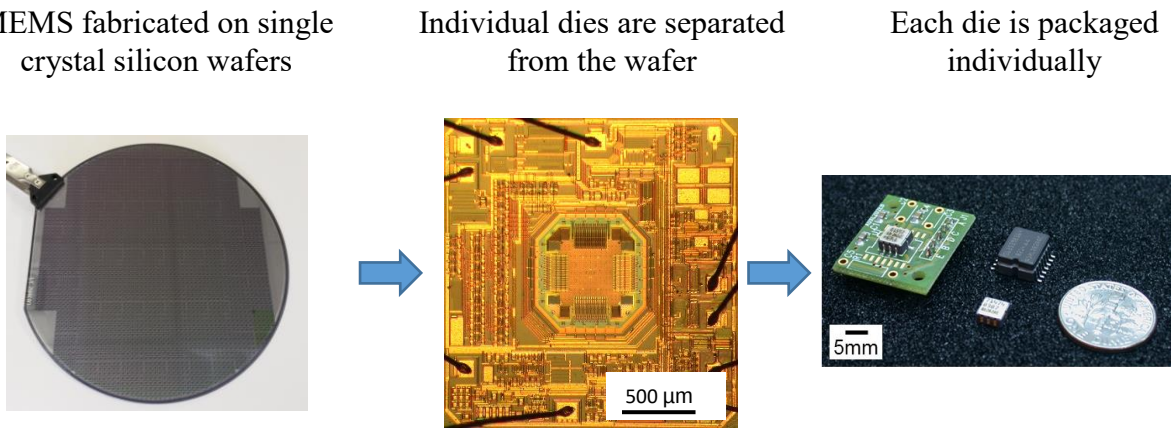

Figure 1. Major stages of MEMS manufacturing process [2]

Many devices come through the process in a faulty condition. The average yield from a 200mm wafer for a MEMS accelerometer is only 85% [3]. This means many devices are packaged and tested unnecessarily. Testing and packaging can be up to 80% of the manufacturing cost of each MEMS device, though this can be very heavily based on device size

and die count [3]. Testing alone was found to take up 25 – 30% of the manufacturing cost [5]. Therefore, if faulty devices could be identified through a form of *in situ* testing prior to the packaging stage there would be major cost saving benefits for the manufacturer.

Given the potential benefits in MEMS manufacturing yields and costs from in *situ testing*, the team wished to develop a tool to conduct such testing. Since material properties of MEMS components are critical to performance, one method of testing would be simultaneous force and displacement measurements. Therefore, the goal of this project was to develop a metrology tool based on force and displacement measurements for *in situ* characterization of the physical properties of MEMS.

2.0 Background

2.1 Operational Theory of MEMSA

MEMSA devices operate by converting acceleration to electrical signals using a variety of physical mechanisms ranging from piezoresistivity, electromagnetism, piezoelectricity, ferroelectricity, optical tunnels, thermal properties, electrostatic charges and capacitance [7]. We focus our research on MEMS capacitive accelerometer designs for their advantages of smaller size and weight, and lower cost of production. In a typical capacitive MEMSA, a proof mass is supported inside the containing substrate by springs or flexible beams. The proof mass has capacitive fingers that are interlocked in-between parallel-plate capacitors fixed on the substrate. When the substrate experiences acceleration, the relative displacement of the proof mass induces a change in capacitance, which can be measured and used to calculate the acceleration of the substrate [8].

An example of a single axis capacitive accelerometer can be seen in Figure 2. The proof mass is constrained to move along a single axis, and is only sensitive to acceleration in this particular direction.

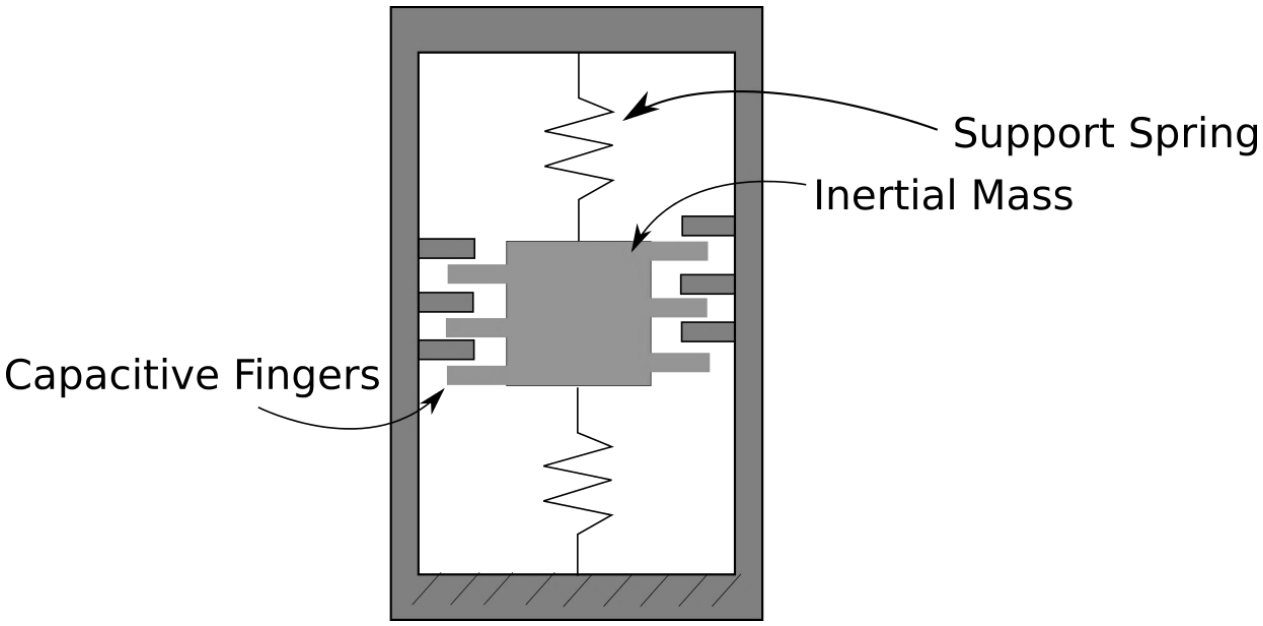

Figure 2. Illustration of the operational theory of a single axis accelerometer

A single axis MEMSA can be modeled as described by Kok shown in Figure 3 [8]. Let

- y denote the displacement of the object that the MEMSA is attached to
- x denote the displacement of the proof mass of the MEMSA
- z denote the relative displacement of the proof mass with respect to the object under investigation
- k denote the stiffness constant of the spring
- c denote the damping coefficient of the damper
- m denote the mass of the proof mass

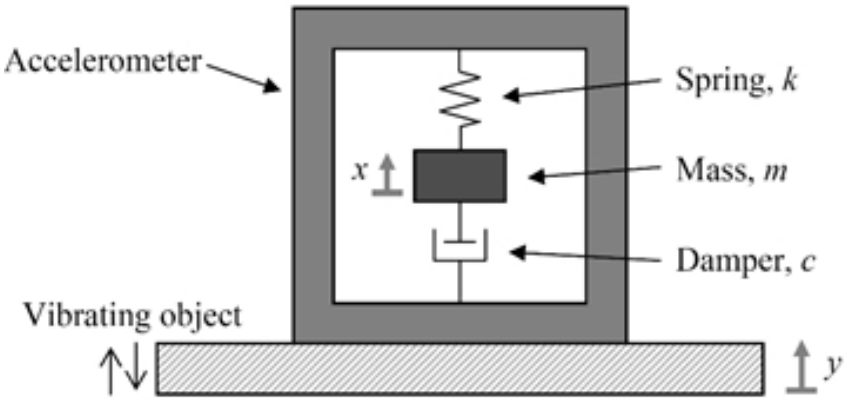

Figure 3. Free body diagram of MEMS Accelerometer [8]

The relationship between these quantities can be modelled by the following equations.

$$z = x - y \tag{1}$$

$$\sum F = m(-\ddot{z}) \tag{2}$$

$$m\ddot{z} + c\dot{z} + kz = 0 \tag{3}$$

If there are multiple identical springs attached to the mass, as often is the case with MEMSA, the effective spring constant of all springs can be modelled in a similar manner. Figure 4 is an example of a single axis MEMSA with four identical springs attached to the mass $k_1, k_2, k_3,$ and k_4. The stiffness constant for springs 1 through 4, are assumed to be identical.

$$k_1 = k_2 = k_3 = k_4 = k_{\frac{1}{4}} \tag{4}$$

the effective stiffness constant k_e for such a setup is given by

$$k_e = 4k_{\frac{1}{4}} \tag{5}$$

Equation 3 now becomes

$$m\ddot{z} + c\dot{z} + k_e z = 0 \tag{6}$$

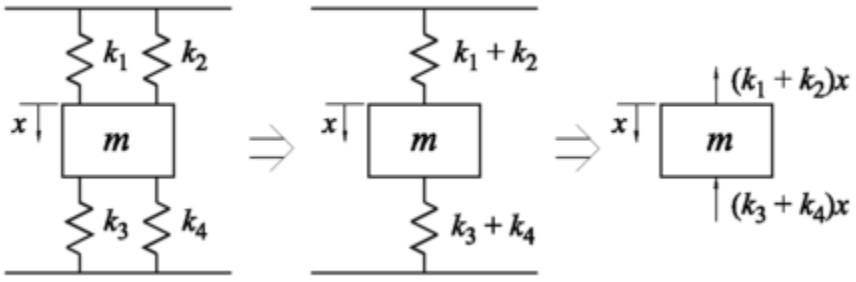

Figure 4. Schematics of a single axis MEMSA with 4 springs

Similar analysis on dual axis MEMSA can be performed by resolving the compound planar displacement into displacement along a single axis, yielding equations like Equation 6.

Both single and dual axis MEMSA measure acceleration by converting acceleration of the proof mass to a change in capacitance. Figure 5 presents a partial view of the proof mass and surrounding capacitive fingers of a MEMSA. C_1 and C_2 represent the capacitance of two parallel plate capacitors fromed by two fixed capacitive fingers attached to the substrate, and a moving arm attached to the proof mass. x_1 and x_2 represent the distance between the top fixed plate and the moving finger, and the distance between the bottom fixed plate and the moving finger, respectively. When the MEMSA is at rest,

$$C_1 = C_2 = C_0 \tag{7}$$

$$x_1 = x_2 = d_0 \tag{8}$$

when the proof mass moves due to external acceleration of magnitude a,

$$\Delta C = |C_1 - C_2| = \frac{2C_0}{d_0}\frac{a}{w_n^2} \tag{9}$$

where w_n is the natural frequency of the spring-damper-mass system.

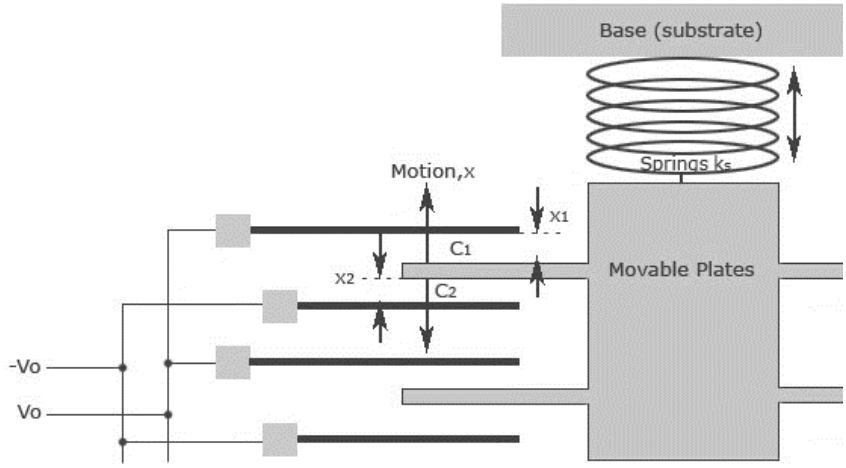

Figure 5. Partial schematic of the capacitors around the proof mass of a MEMSA

2.2 Sources of Errors

MEMS Accelerometer measurements are subject to multiple types of error. Such errors are often the result of flaws in the mechanical design or imperfections resulting from the manufacturing process of a MEMSA. Most MEMSA are manufactured in bulk on silicon wafers. This process is not perfect, and there is a direct relationship between the position of the die on the wafer and imperfections from manufacturing. The farther a die is from the center of the wafer the more likely it is to have flaws. Examples of such errors can be seen in Table 1 [2].

Table 1. A list of some common errors due to mechanical design and manufacturing of MEMSA

Error Type	Description	Causes	Impact
Cross-Coupling	When detected motion along one axis is impacted by motion along an orthogonal axis.	• Spring beam skewing • Spring beam sidewall fraying • Induced stress from temperature variations between anchor points	Loss of accuracy
Spring Constant Error	Some manufacturing errors can cause small changes in the springs found in most MEMSA.	• Residual stresses from manufacturing • Deviations from intended spring geometry • Induced stress from temperature variations between anchor points	Sensitivity errors
Hysteresis	When physical property changes lag behind changes in the controlling effect	• Large impacts • Inner stress and material properties • Structural defects	Bias instabilities and non-repeatable zero positions due to residual deflections
Johnson–Nyquist Noise	Temperature induced white noise	• Thermal vibrations where $V^2 = 4kTBR$ ○ k is Boltzman's constant ○ T is temperature, ○ B is bandwidth ○ R is resistance	White noise
Capacitor Asymmetry	When the gaps between parallel plate capacitors differ across the device	• Wide manufacturing tolerances	Biases in measurements
Orientation Misalignment	Deviations in angle between the MEMSA cap and the inertial mass orientation	• Imperfection in the packaging process	Biases and some cross-coupling

Errors, such as those described in Table 1, can become particularly problematic when an accelerometer is used to approximate position as is often attempted in fields such as robotics and aviation. Table 2 presents a summary of typical types of errors found in the output of MEMSA, and how they contribute to the error in position measurement after double integration with respect to time [9]. If the output errors are unaccounted for, the error in position estimation can grow very rapidly. Therefore, any system that mitigates these errors can dramatically improve the usefulness of MEMSA devices for applications that require high precision.

Table 2. Summary of types of errors in MEMSA output

Error Type	Description	Result of double integration
Bias	A constant bias in the accelerometer's output signal	A quadratically growing position error; $s(t) = \epsilon \cdot \frac{t^2}{2}$
White Noise	White noise with some standard deviation σ	A second order random walk; the standard deviation of the position error grows as $\sigma_s(t) = \sigma \cdot t^{\frac{3}{2}} \cdot \frac{\sqrt{\sigma t}}{3}$
Calibration	Deterministic errors in scale factors, un-orthogonality and accelerometer nonlinearities	Results in a position error that is proportional to the squared rate and duration of acceleration
Bias instability	Bias fluctuations, usually modelled as bias random walk	A third order random walk in position

2.3 Characterization

2.3.1 Impact on Performance

The mechanical properties of MEMSA components have an impact on the device performance. Multiple studies demonstrated that the Young's Modulus of the material and stiffness coefficient play a particularly important role, and these value can be extracted from force measurements [8], [10], [11]. These properties relate to the equivalent stiffness of the supporting springs, which is known to heavily impact both the resonant frequency and the sensitivity of MEMSA as shown in Equations 10 and 11 [10].

$$f_r = \frac{1}{2\pi}\sqrt{\frac{k}{m}} \tag{10}$$

sensitivity can be given in terms of nm/ms^{-2}, which is determined by

$$Sensitivity = \frac{displacement}{acceleration} = \frac{\delta}{a} = \frac{m_{eff}}{k} \tag{11}$$

While the spring design is unique to each accelerometer, folded springs are commonly used thanks to their compact nature. As demonstrated by Wai Chi in Figure 6 the equivalent stiffness of a single folded spring can be determined using Equation 12, where μ is the Poisson's Ratio and t is the out of plane thickness of the beam [10].

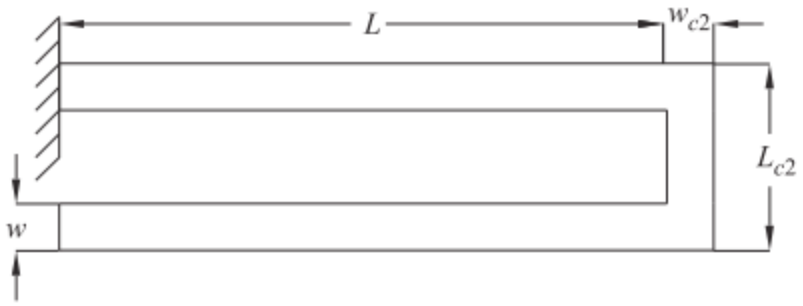

Figure 6. Folded spring model used to develop Equation 12 [10]

$$\frac{1}{k_e} = \frac{1}{Et}\left(\frac{L^3}{2w^3} + \frac{3(1+\mu)L}{5w} + \frac{L_{c2}}{4w_{c2}} - \frac{3LL_{c2}^2}{4w_{c2}^3}\right) \tag{12}$$

This clearly shows the relationship between the Young's Modulus (E) and the equivalent stiffness of the springs. As shown in Equation 13, Young's Modulus is defined as a relationship between applied forces and the resulting deformations of an object.

$$E \equiv \frac{\sigma(\varepsilon)}{\varepsilon} = \frac{F/A_0}{\Delta L/L_0} = \frac{FL_0}{A_0 \Delta L} \tag{13}$$

Equation 13 demonstrates the direct relationship between the material properties of the MEMSA's folded springs and the performance of the device. Additionally, input forces and displacements relate to these properties. Therefore, the ability to measure device displacements and deformations under known input forces can lead to improved characterization and performance of the device.

2.3.2 Previous Methods

The challenge of measuring both force and displacement for system characterization has been approached before. However, none of these systems have used mechanical input on an unmodified device and substrate.

Koo and Ferreira devised a MEMS probe to measure force and displacement simultaneously [12]. The probe was itself a MEMS device, using one set of capacitive combs for sensing and another for actuation. The probe was actuated using the theoretical electrostatic force as given by Equation 14 where n is the number of finger pairs, *h* is the height of a finger, *g* is the gap between two neighboring fingers, and ε_0 is the electrical permittivity of air [12].

$$F = n\left(\frac{\varepsilon_0 h V^2}{g}\right) \tag{14}$$

The stiffness of the device was also evaluated by equating the electrical energy input and the mechanical work done, resulting in Equation 15: Where k is the system stiffness, V is the comb voltage, x is the displacement, C is the capacitance, and C_0 is the capacitance at x = 0 [12].

$$k = \frac{V^2(C - C_0)}{x^2} \tag{15}$$

Using closed loop PID control the system could either control displacement and measure force, or vice versa (b). The stiffness of the probe itself is a factor in the measured stiffness, and must be accounted for in calibration. This calibration was accomplished by using several methods and comparing the results for a high level of certainty. The methods to calculate stiffness were: 1) measuring geometry by microscope, 2) using the distance sensed and the theoretical electrostatic force, 3) equating electrical work and mechanical work to solve for stiffness, and 4) adding known masses and measuring the probe's resonant frequency for each. Resonant frequency was measured by applying an electrical frequency sweep to the actuator.

Although this work measures deformation only at the point of application, it provides insight into working with stiffness and comb drives.

The FT-MPS02 MEMS Probe Station, shown in Figure 7, is a commercially available force probe system designed by FemtoTools. According to its online brochure, it measures force and the probe's displacement, includes a microscope, and has a built in current source and multimeter for electrical stimulus and measurement. It can measure forces ranging from 5 nN to 100 mN and displacements from 1 nm to 15 mm. The coarse motion is accomplished by piezo stepping, whereas the fine motion is accomplished by piezo scanning. It can handle a 200mm diameter wafer, the wafer holding stage can rotate the wafer, and the wafer is held by either clamps or suction. The microscope has a top view and side view which are used for positioning the probe. This side view solves the problem of the probe obscuring the view. Only two orientations are allowed for the probe: in plane and out of plane. The system can create topographic or stiffness maps of an entire surface by probing a large number of points. This process would be much faster if interferometry was used instead and the data was analyzed by software.

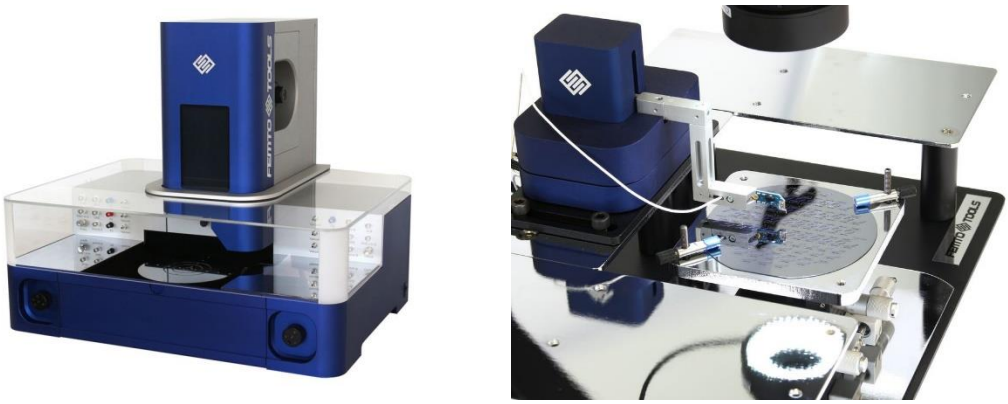

Figure 7. The FemtoTools FT-MPS02 MEMS Probe Station (Left)
FT-MTA02 Micromechanical Testing and Assembly System (Right)

The FT-MPS02 brochure presented a series of example experiments to demonstrate the probe station's capabilities. The examples include: 1) creating a map of a wafer's yield based on probing for stiffness, 2) measuring adhesion forces, 3) cantilever force sensor calibration combined with wafer-level rejection, 4) force of thermal and electrostatic actuators as a time-varying current is applied.

Espinosa, Prorok, and Fischer used another force and displacement method for studying thin films. They fabricated a film of gold on a silicon wafer and etched away the wafer such that the top and bottom faces of the film were both accessible. A nanoindenter applied force on one side, and the deformation of the film was measured from the other side by interferometry [13].

A previous Major Qualifying Project at Worcester Polytechnic Institute entitled *Inverse Method of Nanoindentation by Laser Interferometry* also involves force probing and interferometry [14]. The project is intended for use in material characterization and was validated on a block of aluminum. An atomic force microscopy (AFM) cantilever beam is actuated with a

closed loop piezo. A macroscale arm holds the AFM cantilever to fit it under the interferometer. An interferometer images the deflection of the AFM cantilever as it probes the sample, rather than the deflection of the sample itself. It does so using four phase stepping. A computer program converts these images into displacement data that can be recognized by finite element software. The finite element analysis uses these images to extract the force-displacement graph of the material. No force or displacement sensors are needed for this method. The degrees of freedom include: manual coarse adjustment in X and Y, motorized coarse adjustment in Z, two goniometers that allow angular alignment of the sample, and the piezo that actuates the probe in Z. The interferometer can be removed for other use. The whole system was built for under $5000, and achieves a resolution of 1.23 nm and 0.23 μN.

2.3.3 Proposed Improvements

As described in section 2.3.2 Previous Methods, the problem of characterizing mechanical properties of MEMS has been approached several different ways: probing, displacement measurement, and simulation. Force probes can now apply sub-μN level forces to MEMS [15], [16]. Interferometry has been used to measure the variation in deformation across MEMS surfaces with nanometer precision [17]. Finite element analysis (FEA) has been used extensively to simulate stresses in MEMS devices, sometimes based on interferometry data [18], [19]. However, automated systems which measure applied force and full-field deformation simultaneously are uncommon [12]. Such systems facilitate direct mechanical characterization, diagnosis of failures, improvement of computer models, correlation of device parameters, and improvement of calibration techniques.

Many MEMS operate by sensing changes in capacitance to measure displacements. Accelerometers, microphones, gyroscopes, and pressure sensors have all been implemented this way. These capacitors can also be used as actuators for evaluating the sensor without a force probe [17], [20]. Alternatively, the sensor input, such as acceleration or pressure, can be varied to create the deflections [21]. Mechanical properties can then be estimated from the resulting deformation. However, direct application of force by a probe has the following advantages: the applied force can be known more precisely, force can be applied at any location, and the force is a simple point load rather than a more complicated distributed load.

Based on the merits and pitfalls of characterization methods presented, we propose to design a MEMS metrology tool that applies and measures force using a force probe, and can measure the resultant deformation using interferometry, in order to study material properties of MEMS devices.

3.0 Methodology

To accomplish the team's stated goal of developing a metrology tool for *in-situ* characterization of MEMS mechanical properties using force and displacement measurements, a practical design and testing methodology needed to be followed. Before constructing the prototype, system use requirements were described. Then a sample MEMS device for testing was selected. This device was an ADXL202 accelerometer. To determine system operating constraints analytical calculations and finite element analysis were performed on models of ADXL202 components. These calculations, when combined with the metrology tool use requirements, provided the team with the needed system specifications. The team also determined that, to validate the design, the Analytical, Computational, and Experimental Solutions (ACES) testing methodology would be employed whereby the results would be compared with the previous analytical calculations and simulations to determine data validity.

3.1 Metrology Tool Use Requirements

In order for the metrology tool to be considered truly useful it will need to satisfy the following requirements:

1. System is easy to control with intuitive user interface
2. Can operate within the working distance of needed optical system
3. Controllable with sufficient resolution to operate on and not damage MEMS devices
4. Capable of μN measurements of applied forces
5. Capable of full field displacement sensing with sub-μm resolution
6. Operations are repeatable

3.2 Device Under Test

The metrology tool specifications need to be determined based on an actual MEMS device yet kept general enough so as to be applicable to other MEMS devices. Therefore, a specific Device Under Test (DUT) should first be identified. The metrology tool which the team develops will be initially tested on an Analog Devices ADXL202 accelerometer, shown in Figure 8. This accelerometer was developed for airbag deployment in the automotive industry. This device was selected because the lab in which this project is being conducted has several thousand of these chips.

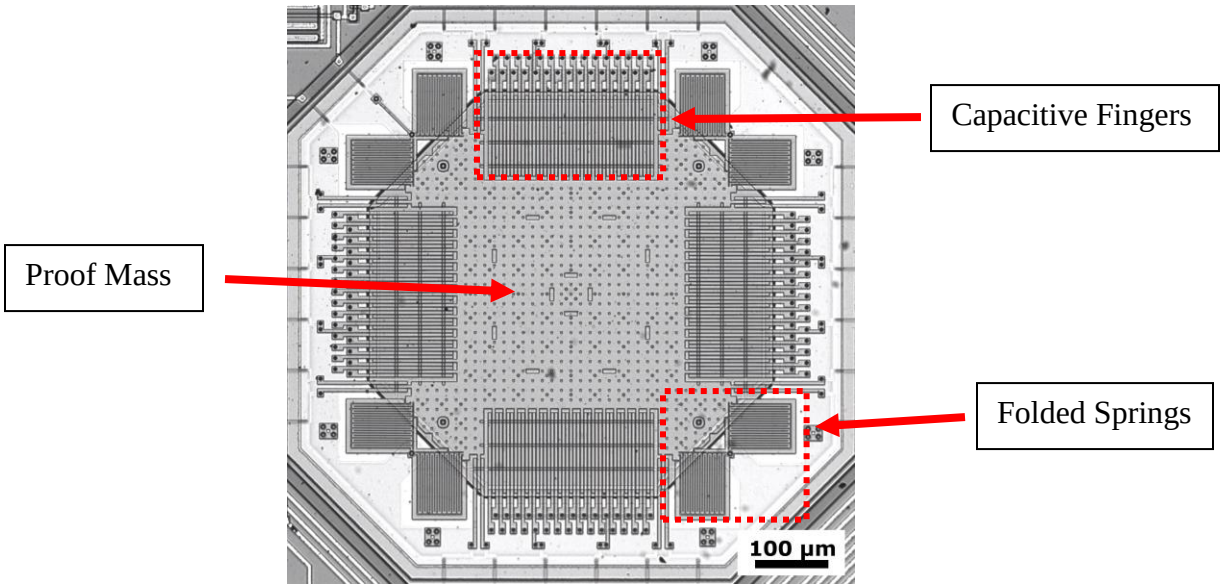

Figure 8. Top view of ADXL202 with features labeled. Taken at 10x optical magnification

The ADXL202 is a dual axis capacitive MEMSA. The ADXL202 inertial proof-mass is suspended 1.6 μm above the substrate by eight folded springs with two at each corner [8]. The four large in plane edges of the mass hold the capacitive fingers, which interlock with the substrate. A number of holes used for chemical release in the manufacturing process can be seen on the mass. The interior square of the proof mass is 309 by 309 μm^2 and, according to company specifications, is 3 μm thick. Proof-mass dimensions were collected using an optical microscope with a measurement resolution of 0.5 μm. This was sufficient for the proof-mass, however, the dimensions of the folded springs were near this resolution and could be a source of error in some of the calculations described.

3.3 Development of Testing Method

As can be seen in Figure 8, there is limited space available on which to apply force for in-plane testing of the ADXL202. The out-of-plane direction, perpendicular to the proof mass, has much more area where a force probe can have clear access. Therefore, the team decided to measure force and displacement in the out-of-place direction, due to the increased feasibility and applicability to wider range of MEMS devices.

To probe the DUT in an out of plane manner requires achieving precise movement on a microscopic scale. Therefore, it is important to outline the motion that the probing tool will use to conduct measurements. The probing approach is comprised of the following steps:

1. The camera detects a point on device and maps its position relative to the probe.
2. A high-resolution stage moves the probe into its target position above the device.
3. Data collection begins

4. Probe actuates along its sensitive axis until a predefined preload displacement is reached.
5. Probe waits for device to settle from impact.
6. Probe descends until target displacement is reached
7. Probe returns to preload displacement
8. Probe waits for device to settle from impact
9. Probe disengages from the device
10. User either ends task or system returns to step 1 for further probing

Using this probing process, the system is able to extract correlated force and displacement data for multiple points on the DUT. In order to ensure that any collected data is accurate, the data should be compared with expectations. To do this the team followed the ACES validation methodology, which compares experimental results with analytical calculations and simulated behaviors.

3.4 ACES Validation Methodology

The Analytical, Computational, and Experimental Solutions (ACES) Methodology, as proposed by Pryputniewicz, was employed to validate the team's results. ACES provides a method to compare expected and experimental results to confirm their validity [22]. ACES breaks the evaluation of systems into three major steps.

First, an analytical model of the device under test (DUT) is created. The resulting mathematical equations represent an approximation of the device. This allows for an "understanding of the general behavior of the component and to estimate the range(s) of anticipated results" [22].

Second, a computational model is created and evaluated often using the Finite Element Method (FEM). This can approximate device behaviors very accurately, but it is still susceptible to error from improper or incomplete model setup.

Finally, experimentation is done on the DUT. This will evaluate the device under real world conditions, but it subject to the imperfections in sensor and actuator designs. Once all three of these steps are completed they can be used to evaluate each other. In this way, a more reliable understanding of device behavior will emerge. A flowchart of the ACES methodology can be found in Figure 9.

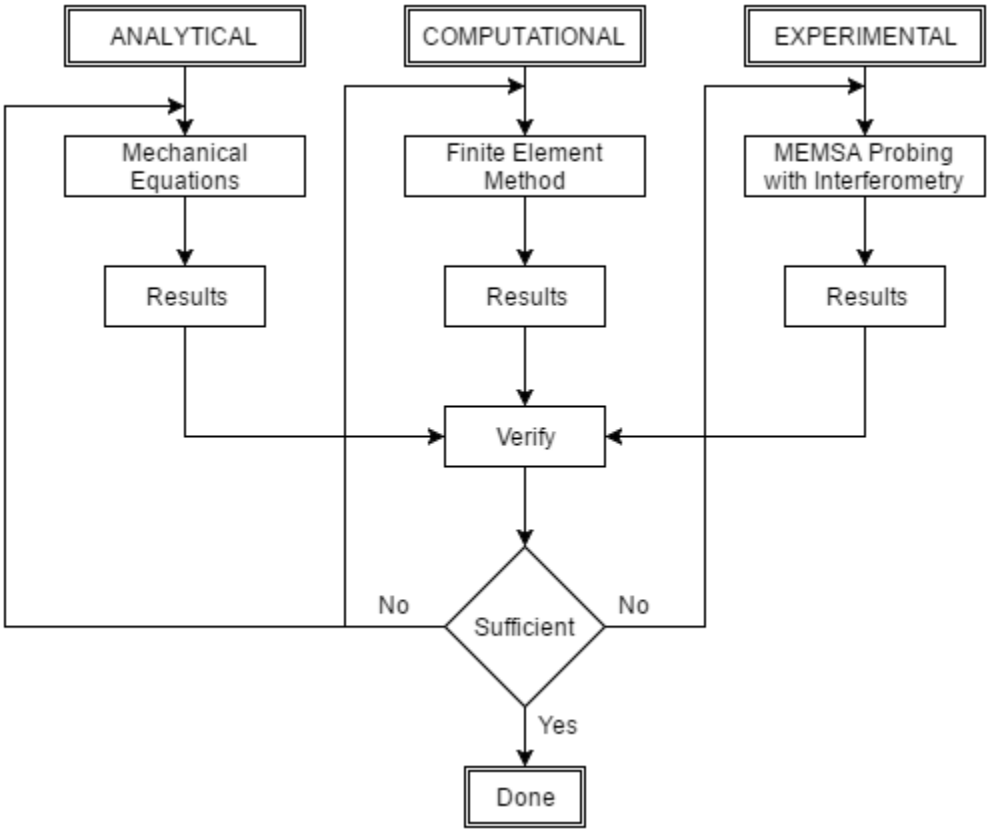

Figure 9. The ACES methodology as it was employed in this project [22]

3.5 Calculation of Stiffness

In accordance with the ACES Methodology, the team used the folded spring model described by Steward in [11] to estimate the equivalent out of plane spring stiffness for the DUT. The impact of out of plane forces on a folded spring can be analyzed using the relationship between geometry and material properties of a folded spring [11].

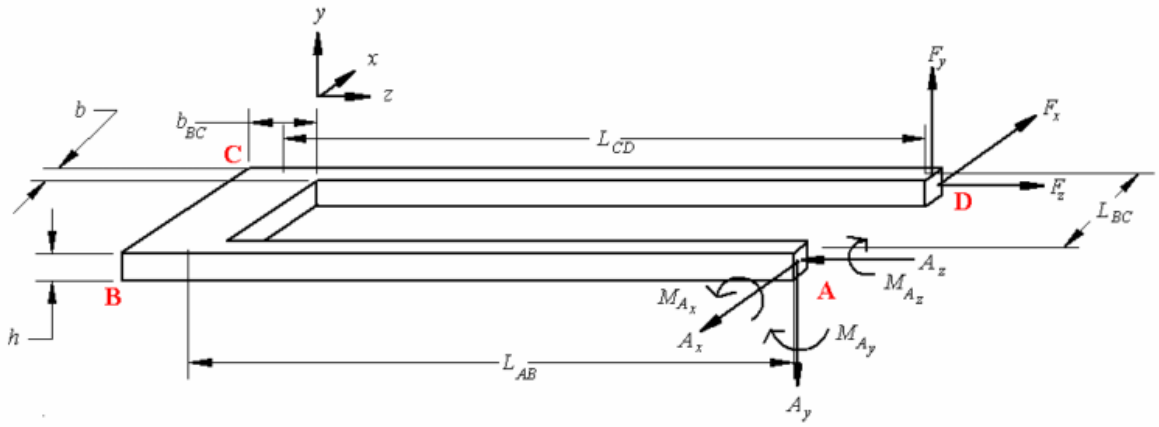

Figure 10. Free body diagram of a folded spring [11]

In the setup represented in Figure 10, y-axis is the out-of-plane direction. L_{AB}, L_{BC}, L_{CD} represent the length of sections AB, BC and CD; F_x, F_y, F_z represent the force applied in x, y and z direction. E is the modulus of elasticity, G is the shear modulus, J_b is the polar moment of inertia for sections AB and CD, A_b is the cross section area of sections AB and CD, A_c is the cross sectional area of section BC, I_{cz} is the moment of inertia for section BC in the out-of-plane

direction of motion, c_1 is the torsional coefficient of a rectangular beam [23]. Δ_{D_y}, the displacement in y direction at point D in Figure 10, is given by the equation [11]:

$$\Delta_{D_y} = \frac{F_y}{3EI_{bx}}(L_{AB}^3 - 3L_{AB}^2 L_{CD} + 3L_{AB}L_{CD}^2)$$

$$+\frac{6F_y L_{AB}}{5GA_b} + \frac{F_y L_{BC}^2 L_{AB}}{GJ_b} + \frac{F_y L_{BC}^3}{3EI_{cz}} + \frac{6F_y L_{BC}}{5GA_c} + \frac{F_y L_{CD}^2 L_{BC}}{GJ_c} + \frac{F_y L_{CD}^3}{3EI_{bz}} + \frac{6F_y L_{CD}}{5GA_b} \qquad (16)$$

Using Equation 16, the calculated equivalent out of plane stiffness for the DUT was 22μN/μm. See Appendix III: Folded Spring Stiffness Calculation for MATLAB calculation. According to this stiffness, to push the proof mass a displacement of 0.5μm should result in a measured force of 11μN. The material properties of polysilicon which were used for this calculation can be seen in Table 3.

Table 3. Material properties used for calculations of stiffness with ADXL202 accelerometer

Property	Value	Units
Density, r	2.33	g/cm^3
Modulus of elasticity, *E*	160	GPa
Poisson's ratio, m	0.23	dimensionless

3.6 Finite Element Analysis

After conducting analytical calculations, the team performed a finite element analysis (FEA) as a comparison. In FEA a computer software is used to subdivide a 3d model of the relevant part into thousands of individual elements. Then the deformation and stresses on the system are calculated element wise across the whole structure. This provides an accurate approximation of the real-world deformation. However, the method is dependent on accurate selections of material properties and mass dimensions.

To conduct the FEA a CAD model of the ADXL202 proof-mass was created using Solidworks. The dimensions of the proof-mass and springs are the same as those described in Section 3.2 Device Under Test. With the CAD model created the team loaded it into the FEA software ANSYS for analysis. A ramping input force from 0 to 100 μN was then applied to the center of the proof-mass. This created the graph of maximum displacement and input force shown in Figure 11. An exaggerated representation of the deformation of the system can be seen in Figure 12. As shown, the folded springs are the primary source of deformation in the system while the proof mass undergoes the largest absolute displacement. From the data calculated by ANSYS the expected equivalent stiffness of the system is 8.2 μN/μm. The discrepancy between this value and the analytical calculations could be due to changes in system mass on the CAD model and the analytical calculations not accounting for deformation within the proof mass itself.

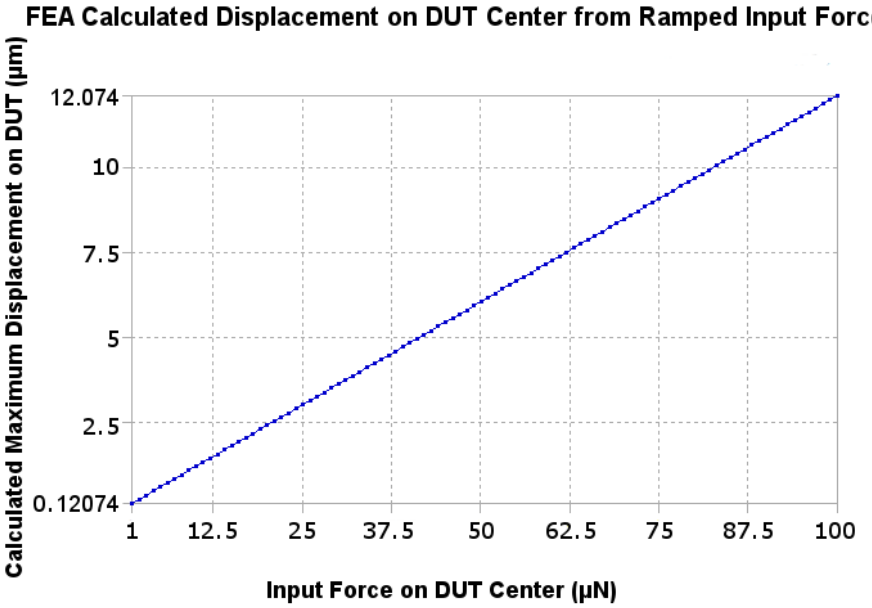

Figure 11. Calculated maximum displacement on the ADXL202 proof mass from a ramped input force at device center

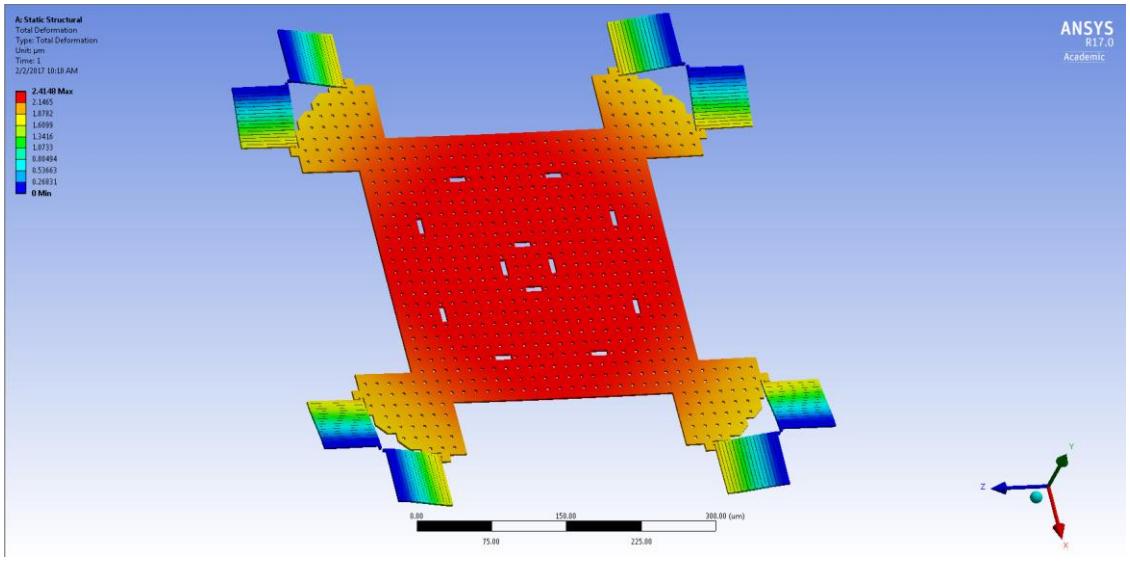

Figure 12. Exaggerated representation of the deformation of the ADXL202 accelerometer from an input force at its center as calculated by FEA with ANSYS. Color ramp represents the total displacement across the system

3.7 System Constraints

The use of FEA and analytical calculations provided the team with not only a way to compare results with expectations, but also bounds on the levels of forces which would need to be measured and the necessary resolutions of actuators. When combined with the measured dimensions of the DUT, a full set of target system specifications could be developed. The target system specifications and those of the final prototype are shown in Table 4 and

Table 5.

Table 4. The target system ranges and resolutions
based off of the preliminary calculations and DUT measurements

Sub-System	Target Range	Target Resolution
Coarse Z-axis actuator	±15 mm	2 µm
Planar positioner	200 µm	0.5 µm
Fine Z-axis actuator	20 µm	1 nm
Camera (10x)	N/A	0.5 µm/pixel

Table 5. The achieved system specifications of the final prototype

Sub-System	Range	Resolution	Actuator Used
Coarse Z-axis actuator	25.4 mm	0.12 µm	MM-3M-F.1 Linear Stage
Planar positioner	150 mm	0.5 µm	TS Series Linear Stages
Fine Z-axis actuator	20 µm	5 nm	PAZ 005 Piezo Actuator
Camera (10x)	N/A	0.74 µm/pixel	AVT Pike-F100B

4.0 Implementation

The final prototype which was constructed can be broken down into four major components: a user interface, systems for positioning, optical sensing, and force measurement. An overview of how these systems interface with one another can be seen in Figure 13.

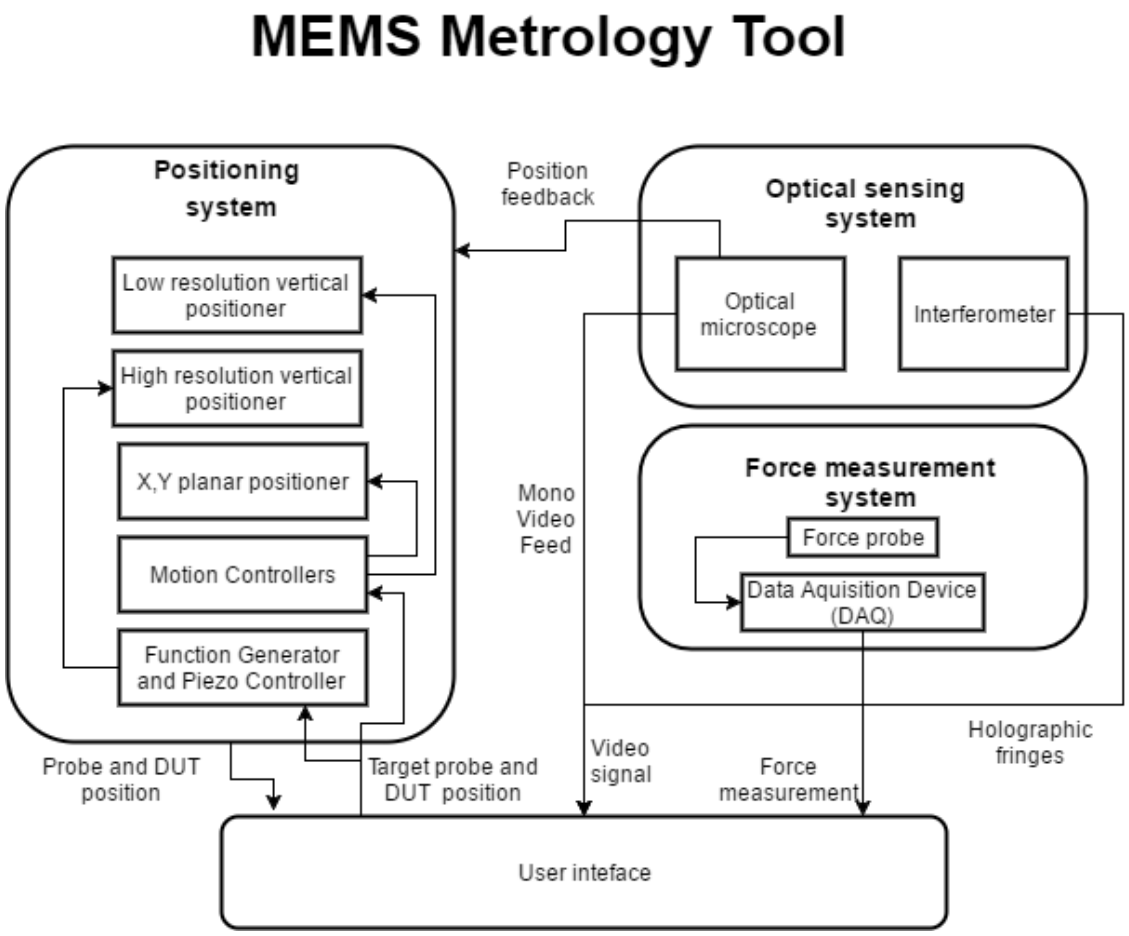

Figure 13. MEMS Metrology Tool Prototype component diagram

The system is controlled through Graphical User Interface (GUI). This is used to communicate user commands to the motion controllers as well as display current position information and a live video feed from the interferometer. The commands from the user interface are processed by three motion controllers which operate each of the system's actuators. Additionally, from the GUI the user can calibrate the system for future automated probing operations. Data collected by the force probe during the automated probing process is collected with a USB-Data Acquisition Device (DAQ). The force probe output is filtered using a custom filtering circuit to remove noise. The final data is graphed in MATLAB figures for analysis. The actual force probe, positioning components, and optical components can be seen in their final configuration in Figure 14.

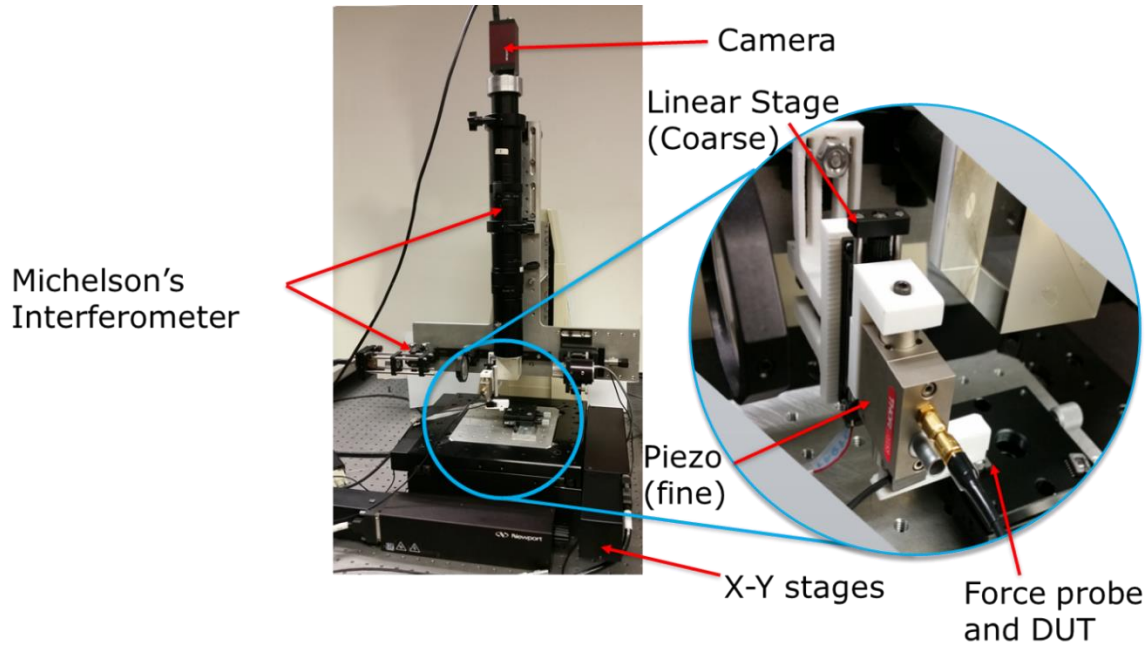

Figure 14. Major components in the positioning and optical sub-systems of the prototype

4.1 User Operation

The team's prototype is operated with a custom GUI, which was designed to facilitate easy operation of the system. The GUI allows the user to calibrate the system, capture video and images, run a probing sequence, and manually control the actuators. The final GUI can be seen in Figure 15.

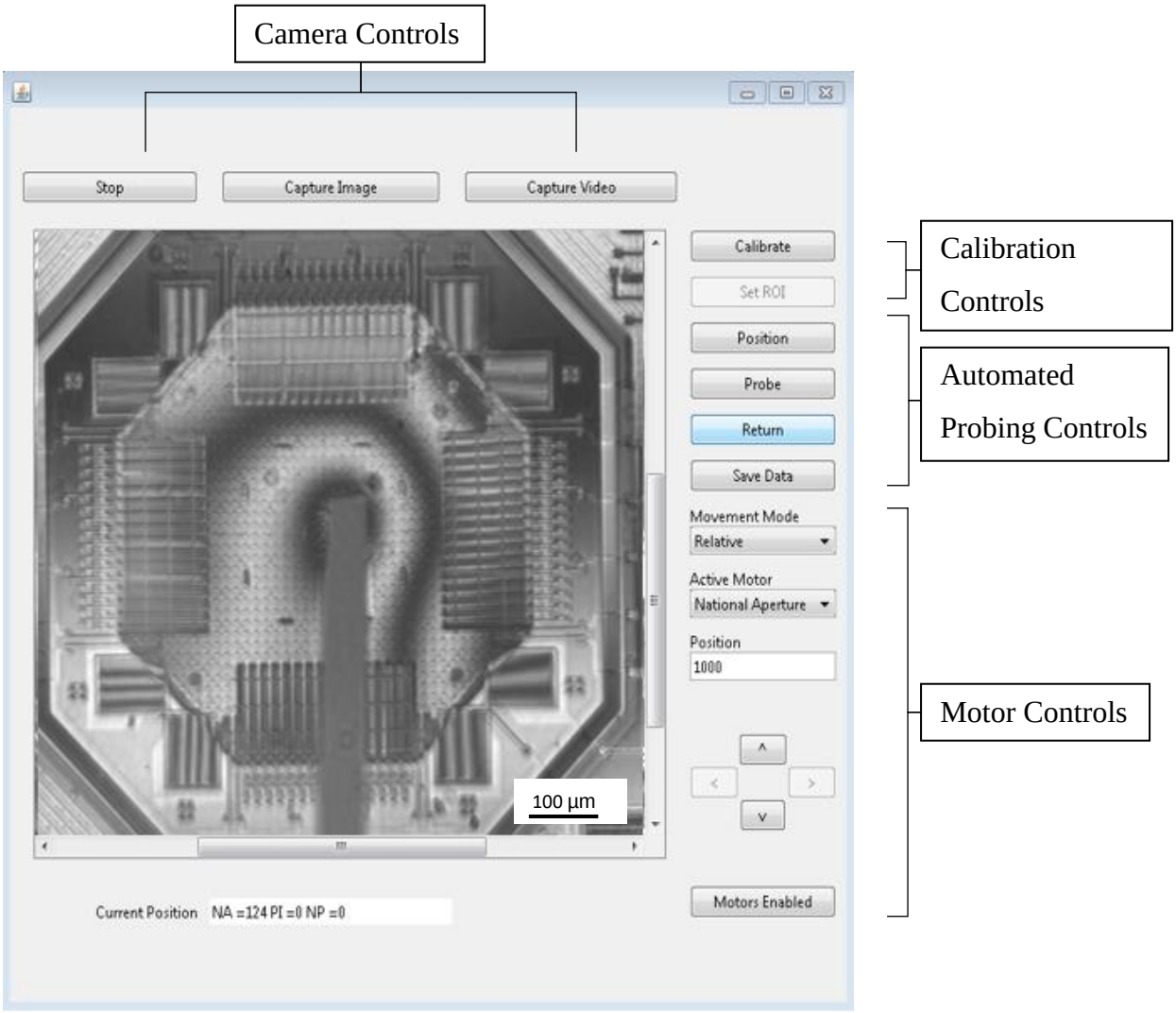

Figure 15. The Graphical User Interface (GUI) used to control the Metrology System

The user operates the system using a straight forward process starting with system initialization then calibration and finally automated DUT probing. A high-level overview of the operation flow can be seen in Figure 16. A user manual is also provided in Appendix I: User Manual.

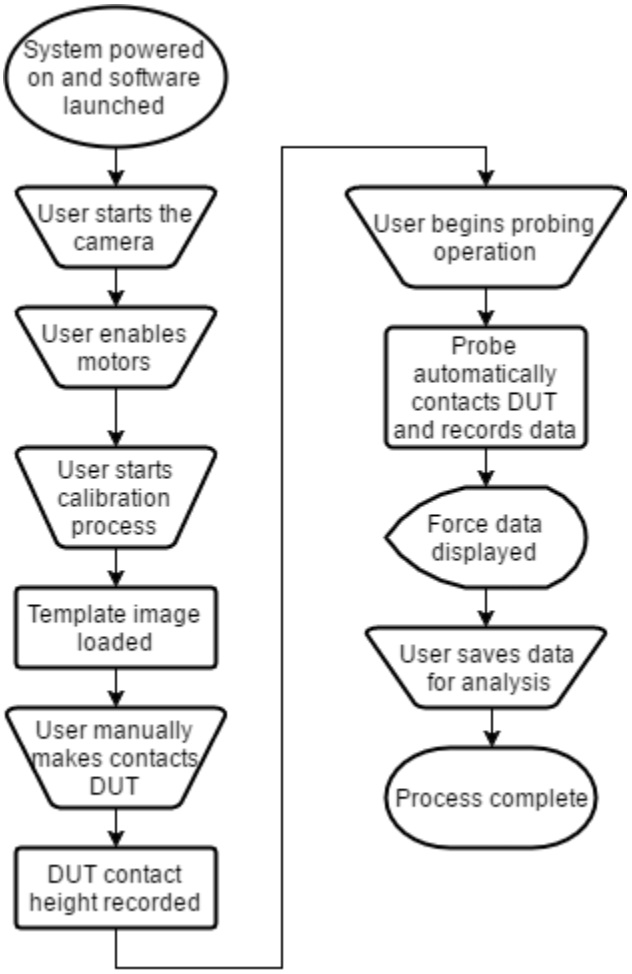

Figure 16. Flowchart of standard system operation

4.2 Software Design

The software which operates the metrology system prototype, has two major components the front-end GUI which accepts user inputs and displays data, and the backend operational code which interfaces with the various sensors and motion controllers in the system. The software design of each is discussed in further detail in following sections. Object oriented programming design (OOP) concepts were applied to both the front-end and back-end software components to facilitate easy future expansion. OOP is the design practice of separating conceptually distinct portions of code into discrete classes. Where each class stores data necessary to describe its state or behavior and contains methods which operate on this data. The ability to instantiate multiple independent objects of each class allows for the programmer to develop data structures and program flows which follow conceptually simple patterns without rampant rewriting of code. Additionally, OOP allows for easier future code modification through concepts like encapsulation and abstract classes. For these reasons, among others, the team developed our software using this industry standard paradigm.

Along with selecting a program design methodology, the team also needed to determine what language to use for the software itself. MATLAB was selected as the primary language for its easy data visualization and acquisition capabilities. However, MATLAB has limited graphical interface capabilities so the GUI was instead implemented in Java using the Swing library. While MATLAB worked well for initial testing purposes, it proved cumbersome due to an unintuitive OOP syntax and memory limitations. The use of a 32-bit Windows machine limited MATLAB's available memory to a fraction of 4GB depending on other operating programs. This memory space was quickly eaten up by the memory heavy MATLAB toolboxes specifically the Data Acquisition and Image Acquisition Toolboxes. This led to many out of memory errors during

development which were unpredictable and hard to debug. Using an alternative language like C++ or Java would have allowed us to overcome these limitations more easily through smaller overhead and greater control of system resources. Fortunately, the final system could function within the necessary memory constraints.

4.2.1: Java MATLAB Interface

The GUI interface can communicate with the MATLAB back-end thanks to MATLAB's internal Java Virtual Machine. Since Java objects can be interacted with in MATLAB the coordination of the Java view class is straightforward. The Java GUI code is saved as an executable JAR file when it is compiled. This JAR file is then loaded into MATLAB when the software is launched. This JAR contains a main class which has getter methods for each of the Java Swing objects which represent the components of the GUI such as buttons. By calling these getter methods each component can be accessed directly with MATLAB. At this point the custom `MainView` MATLAB class implements all the event listeners for each component of the GUI. At this point, MATLAB is used for the remainder of the program operation.

4.2.2: MATLAB Backend

The MATLAB software controls and interfaces with the many components of the team's prototype. The primary logic which controls the automated probing process and motor control is located in the `MainModel` class. This class's methods are called on user action from the `MainViwew` class which interfaces with the Java GUI. The `MainModel` class stores an object representing each of the sensors and actuators used in the prototype. The classes which connect to these components were created using a class hierarchy in accordance with OOP design. In this

hierarchy, each physical component extends an abstract Equipment class and other abstract child classes as needed. A simplified class diagram of this structure can be seen in Figure 17. The full class diagram can be seen in Appendix II: Software Design.

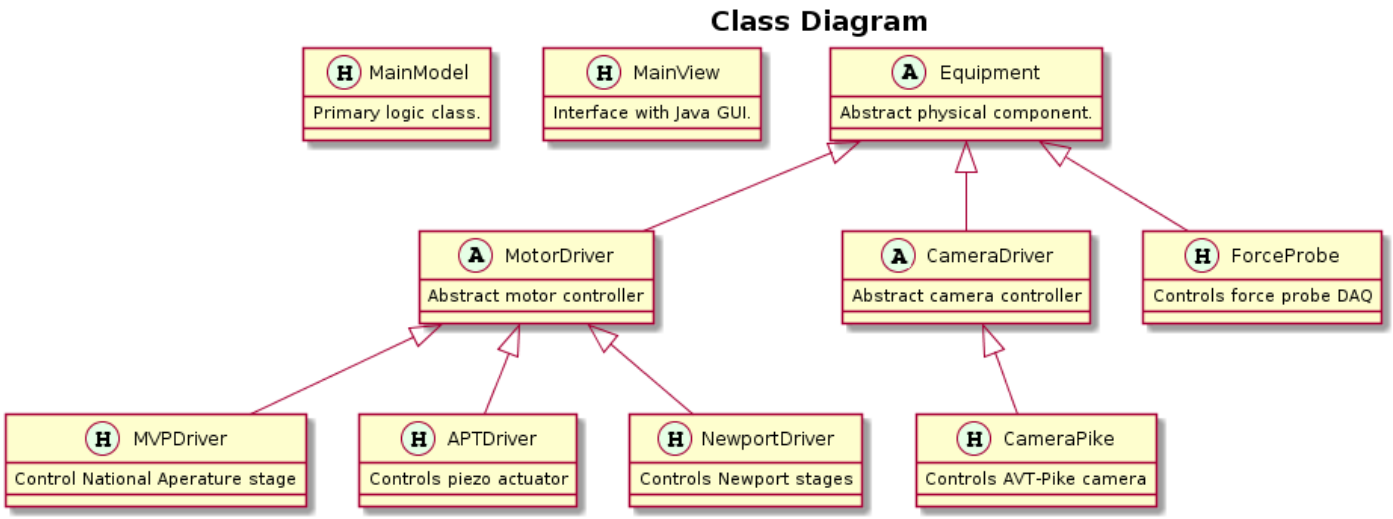

Figure 17. Abriged class diagram of controlling software

The main program has three main forms of operation: manual jogging, calibration, and automated probing. The default mode on system startup is the jogging mode. This allows the user to enable motors and control each motor individually. The calibration process is launched when the user hits the calibration button. This allows the user to select a template image to use for planar positioning and determine the height of the DUT through manual probing. Once the calibration process has been run the user may begin an automated probing run. This will probe the DUT and record the force and displacement data. A state diagram of these modes can be seen in Figure 18.

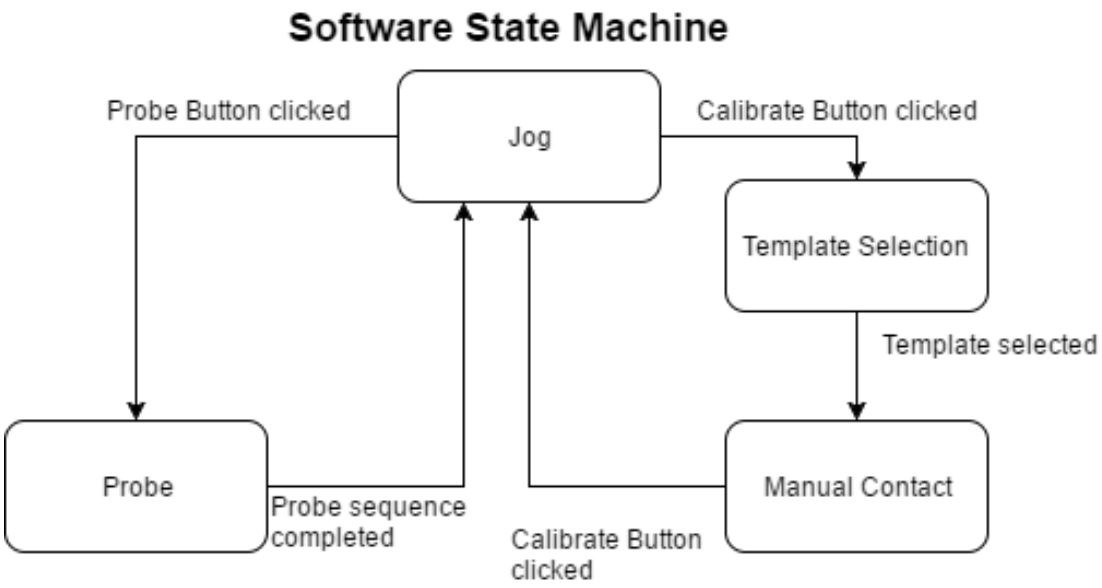

Figure 18. Stage machine schematics of the software

4.2.3: Automated Probing

Once a user has performed the calibration process and positioned a DUT, the automated probing process can begin. The algorithm for this process starts with the coarse motion of the probe towards the device followed by an iterative increase of piezo location until contact it made. Once contact is detected, continuous data collection begins and the function generator is triggered. This creates a ramped input voltage to the piezo which induces a corresponding displacement on the probe. Once the probe reaches the maximum input displacement, it retracts at the same rate. This process is repeated for the desired number of points on the device. The process follows the flow shown in Appendix II: Software Design.

4.3 Optical Sensing System

Several types of interferometers were available in the CHSLT. A Michelson interferometer was chosen because it provided an appropriate magnification of 10x and included a large enough working distance that has 46 mm clearance between the object and the beam splitter, which is the lowest part of the optical sensing system. The Michelson Interferometer had been assembled with the optics mounted to a custom back plate by Ryan Marinis who was a previous graduate student at CHSLT. A Michelson Interferometer operates as follows: 1) a beam from a coherent light source is split in two by a beam splitter, 2) one half beam reflects off of the DUT and the other reflects off of a flat reference mirror, and 3) both half beams recombine forming an interference pattern that is recorded by the camera. The interference fringes form contour lines, similar to those in topographical maps. This is because the path length difference between the DUT and reference mirror beams determines whether the interference at that point will be constructive (white) or destructive (black). See Figure 19 for process diagram.

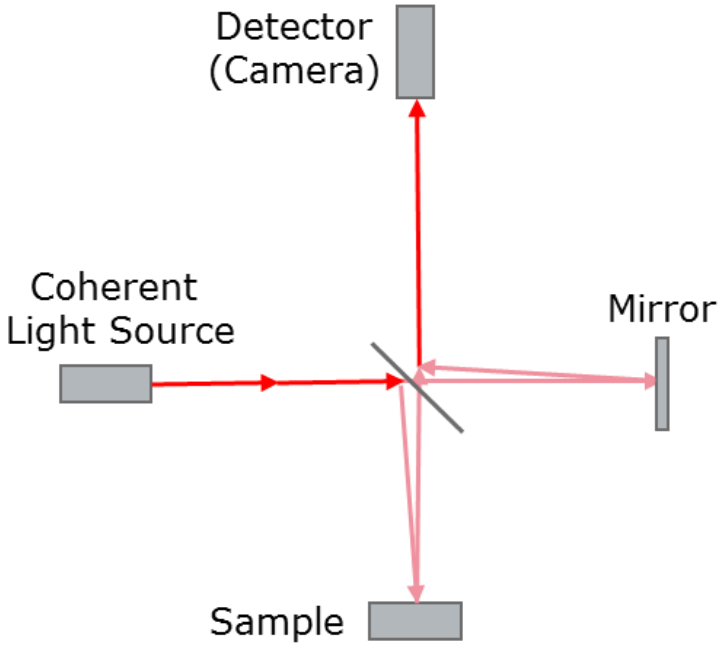

Figure 19. Schematics of a Michelson Interferometer

To align the interferometer, the camera was removed and the lights were turned off so that the sample beam and the reference beam mirror made red spots on the ceiling. Then the beam splitter was rotated until the two dots aligned. After this process, we could obtain noticeably higher contrast in the fringes.

The original plan was to use four phase stepping to extract high resolution measurements from the interference patterns. Four phase stepping involves taking four images, each image with the phase of the light offset by 90 degrees by stepping the piezo. The information from these images can be used to solve for sub-wavelength displacements. Four phase stepping had already been implemented in a software called LaserView. After struggling to get meaningful results, the team concluded that four phase stepping was not essential to the project and could be

implemented in future work. In our system, the purpose of the interferogram is to allow the operator to visualize when and how contact is made and conduct an analysis on the image if the operator has the technical knowledge.

The interference pattern created by interferometry makes the usage of classical computer vision techniques more challenging due to the large changes in contrast present on the video feed. The team experimented with ways to resolve this issue and determined that a method of removing fringes from the image during image processing steps would achieve the best results. To do this, the piezo behind the mirror was actuated so that the optical path difference would be greater than the coherence length, removing the fringes. The piezo controller input was 10V, but the max DAQ output was only 5V, so we had the DAQ operate a switch connected to an external power supply using an IRF520 MOSFET, as shown in Figure 20. Unfortunately, there was not enough time to fully integrate this feature into the final system. However, the method was demonstrated to be viable and should be pursued as future work to improve the system.

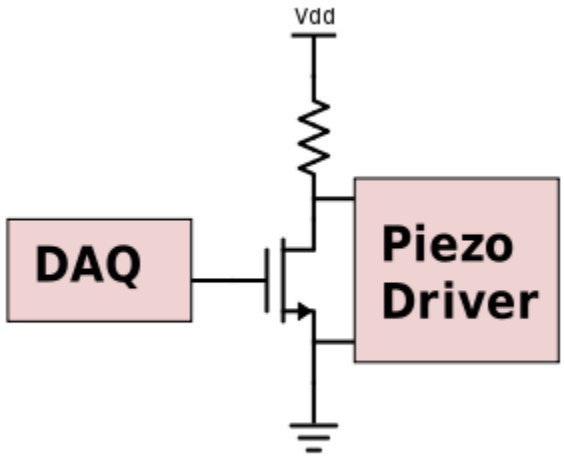

Figure 20. Schematic of circuit to control phase stepping

4.4 Camera and Computer Vision Technique

4.4.1 Hardware and Integration

A camera is needed to digitize the image created by the Michelson Interferometer in order to further visualize the process and quantify the resulting interferogram. In our system, we used an Allied Vision Pike F100B Camera to image the operation on the DUT. The camera uses a charge-coupled device (CCD) to digitize incoming light, and can output 10-bit monochromatic images at 1000 by 1000 pixels at up to 60 frames per second, generating up to 60 Mb of data per second. Each pixel on the CCD is 54.76 μm^2 (7.4 µm by 7.4 µm), which represents 0.5476 μm^2 (0.74 µm by 0.74 µm) on the DUT when operating at 5x magnification [24]. The camera communicates with the controlling computer via 1394b FireWire interface, which has a theoretical maximum bandwidth of 800 Mb/s, sufficient for data transfer at the frame rate that we are operating at.

Like the other components, the camera is integrated with the controlling software through MATLAB. Specifically, we made use of the Image Acquisition Toolbox in MATLAB to initialize communication with the camera and to capture frames from it. The Image Acquisition Toolbox works with a wide range of devices including FireWire cameras, USB cameras and specialized high-speed cameras. It provides a uniform interface to control imaging parameters such as frame rate, exposure, white balance, and contrast. We utilized the Image Acquisition Toolbox to design a custom abstract class for camera objects. The class object, called `CameraDriver`, stores the parameters such as magnification, size of pixels, and has functions for starting and stopping the camera, acquiring images, and changing imaging parameters. Specific object instances were then derived from the abstract classes, filling the data fields using concretes intrinsic parameters of the camera. This technique was tested on both the Pike F100B

camera, as well as an integrated USB webcam, and has successfully provided us with one unified interface for when we want to develop and test on our laptops, and when we want to conduct experiment on actual lab equipment, maximizing code reuse. Should the CHSLT lab decide to use other imaging devices in the future, the program will have the flexibility to adapt to such changes.

4.4.2 Determining Distance from Probe to Device

A critical piece of information needed to safely conduct tests on the DUT is the vertical (out of plane) distance from the probe to the DUT. When the actuators are fully retracted, this distance could be up to 46 mm; yet we also need to be able to sense if the probe has reached within 20 µm above the surface of the DUT, in order to stop the coarse actuator and engage the fine actuator, to avoid overshooting and damage to the probe. Additional complexity arises from the small size of the tip of the probe, which is a 50 µm by 50 µm square. Distance sensors that have the desired accuracy and works with such small objects are hard to obtain. Therefore, we sought to address the distance estimation issue using video input from the camera.

During operations of the system, the relative distance between the optical sensing system and the DUT remains fixed, while vertical positioners move the probe up and down to make contact with the DUT. When the probe is far from the DUT, it appears blurry on the video input. Clarity of the probe in the video input increases as the probe moves closer to the DUT, and eventually achieves the same sharpness as the DUT right before making contact. Quantifying the sharpness of the blurb of pixels that represent the probe can therefore allow us to estimate the distance from the probe to the DUT. Computer vision technique based on the variance of Laplacian have been successful at determining if an image is in focus [25]. It works by

calculating the variance of the Laplacian of the image. A larger variance indicates sharper focus, whereas a small value indicates that the image is not well focused. Figure 21 demonstrated how the appearance of a sharp object and the variance of Laplacian changes at varying distance away from the home position of the vertical actuators. We conducted tests to study the feasibility of the variance of the Laplacian methods on a manually rectangular region in the video input that contains a medical needle that resembles the force probe in appearance (actual probe was not used for testing purpose for safety concerns). 25 sample displacements away from the home position of the vertical actuators were selected, ranging from 0 (at home position) to 17500 encoder ticks (2170 μm) (near device contact), in steps of 700 encoder ticks (86.8 μm), were tried. The variance of Laplacian for the bounding box containing the needle was calculated, and plotted against displacement along with the best exponential fit, as shown in Figure 22. The correlation between displacement and variance can be readily seen. The variance value could in theory be used to estimate the proximity of the probe to the DUT.

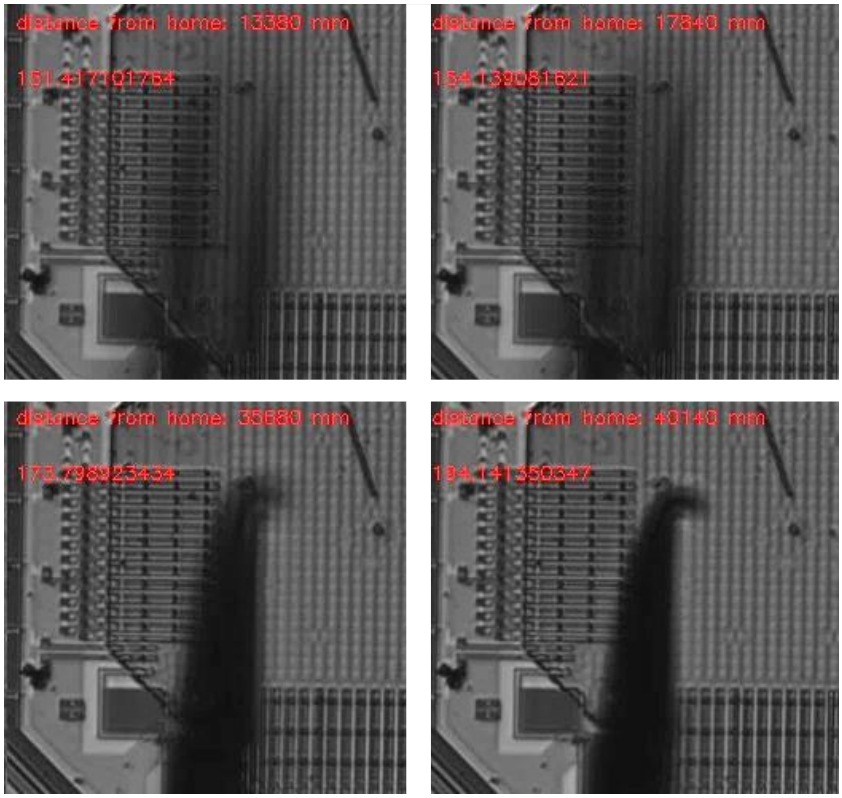

Figure 21. Set of four images demonstrating increase in focus level of a sharp object (surgical needle) in view of the interferometer as the object approaches the focal plane of the interferometer. Numerals in the images represent variance of Laplacian for the region of interest

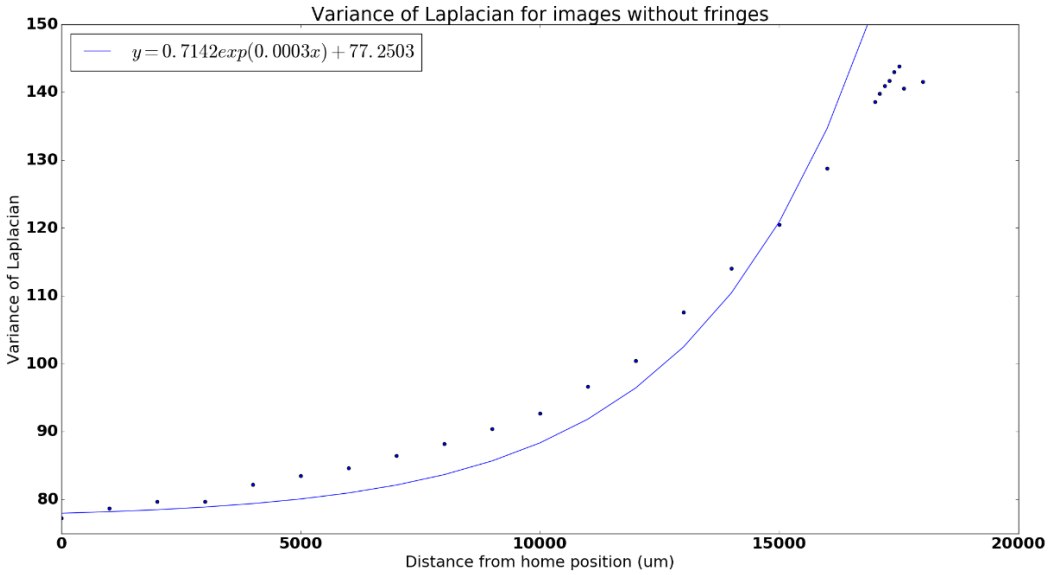

Figure 22. Variance of Laplacian of needle bounding box at various height

However, some practical challenges made it difficult to adopt variance of Laplacian for fully automated testing. Although the trend of the relationship between the variance of Laplacian and displacement remains qualitatively similar, the numerical variance score depends largely on the background and illumination. Each time the DUT shifts location, causing the appearance of the background image to change, the calibration curve that relates variance of Laplacian to displacement needs to be re-calculated. As we frequently had to readjust the position of the DUT during the testing and development phase, the calibration phase became too time consuming. We therefore decided to use changes in the interferometric fringes to manually detect if contact has been made as an initial calibration step. The MATLAB function that performs the variance of Laplacian calculation is left in the code repository for future reference.

4.4.3 Determining Planar Displacement of the DUT

In order to generate an accurate stress map of the DUT from probing multiple points on the device, it is necessary to assign a coordinate frame to the device and determine the probing location in the plane of the device relative to the origin of the assigned coordinate frame. Although the Newport planar actuators that controls the X-Y motion have encoders and can report the number of encoder ticks which can be converted to amount of planar displacement, each encoder tick is 0.5 μm. However, the planar stages also suffer from backlash, making accurate determination of displacement from encoder counts unreliable for our application, and the planar actuator only has ±6.0 μm accuracy.

On the other hand, one pixel of the Pike F100B camera corresponds to 0.5476 μm^2 (0.74 μm by 0.74 μm) on the DUT when operating at 10x magnification. Counting the relative planar displacement in pixel units using the camera would achieve the desired accuracy. Several computer vision techniques to efficiently track features of an input image exist. Amongst them, template matching is an efficient method for tracking regions of interest across frames. Template matching requires a reference template image and an image stream as input, as is able to scan the image stream to find occurrences of the template image, and report a bounding box of the best match. When given the image of the proof mass as well as camera feed as input, template matching is able to accurately and repeatedly locate the proof mass, as shown in Figure 23. Template matching also works well under poor illumination conditions. Since the probe would be operating above the probe and obstructing the view of the DUT, we also tested template matching with partial obstruction of the feature being tracked, and found template matching to work well. Although template matching would fail when the scale of the feature changes, the

magnification in our setup remains constant hence this would not affect the usability of template matching for our purpose.

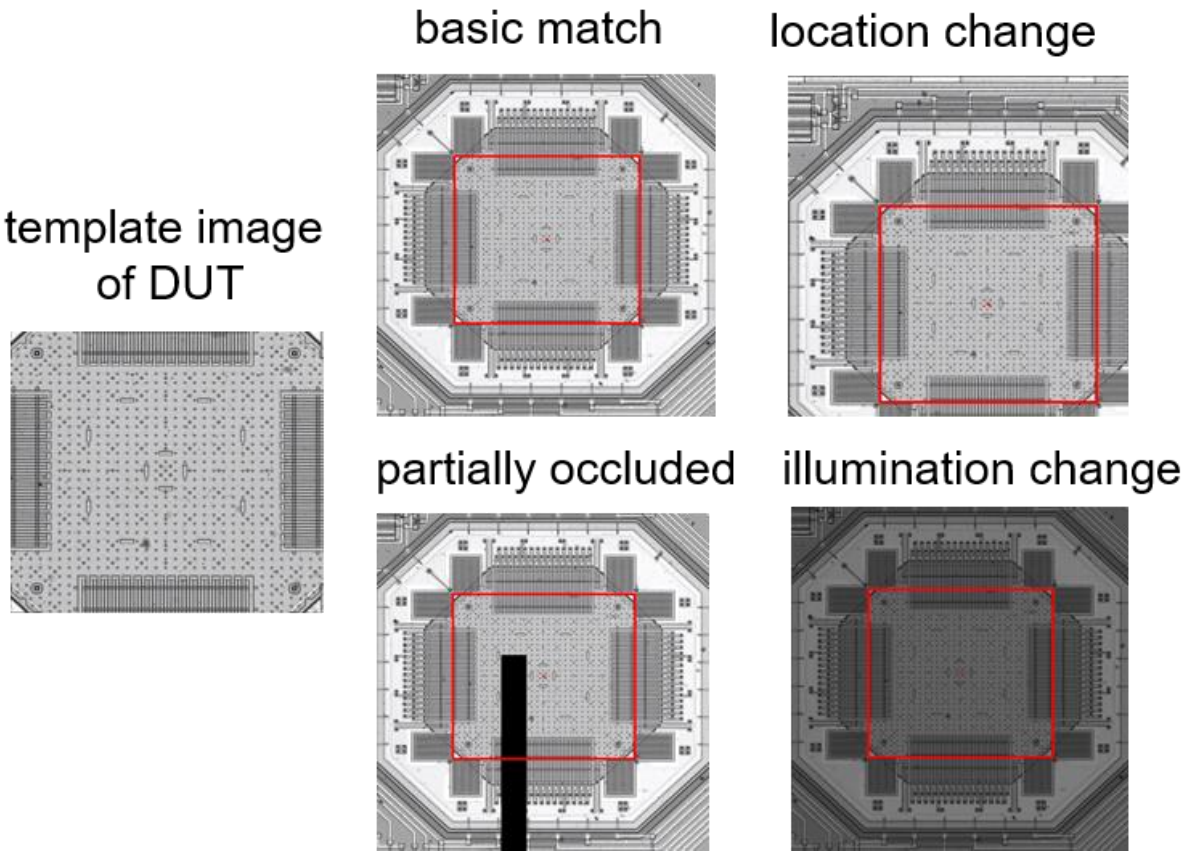

Figure 23. Template matching under a variety of imaging conditions

When implemented correctly, template matching can run at rates well above 60 Hz. However, MATLAB's implementation of template matching suffered from performance issues. As a result, we adopted OpenCV's implementation of template matching to mitigate the performance issue [26]. A template matching function was written in C++ to call OpenCV's

implementation of template matching. The C++ script was then compiled using the MEX compiler in MATLAB R2015A into a binary .mex file that can be accessed by MATLAB programs. By relying on a more efficient implementation of template matching, we were able to track the location of the proof mass of the DUT across every incoming frame, which allowed us to estimate displacement of the DUT with a resolution of ±1.05 μm.

4.5 Planar XY Positioning

In order to allow for accurate probing of any point on the DUT, a sufficiently accurate positioning system for XY planar motion was needed. As determined by the desired system specifications, the motion positioner would need to provide a minimum range of 309 μm in order to allow any point on the DUT to be reached by the force probe. Since the positioning feedback would be provided by the vision system, the image resolution and magnification limited the minimum resolution of the positioner. As discussed in section 4.4.1 Hardware and Integration, the vision system provided a physical resolution of 0.74 μm/pixel. Therefore, the desired positioner needed to be in a comparable range. In the lab, a pair of Newport TS-Series Linear Stages were available, see Figure 24, which satisfied these constraints having a range of 150mm and a resolution of 0.5 μm. This positioner was controlled with a Newport ESP6000 Universal Motion Controller. The controller communicated with the operating software through proprietary Newport PCI connector and C++ Dynamically Linked Library (dll). The dll was loaded into MATLAB in order to interface with the GUI. Unfortunately, the drivers for the controller were only compatible with 32-bit Windows Operating Systems. Usage of 32-bit Windows would limit the amount of Random Access Memory (RAM) available for use by the operating software.

While the final software could operate within these limits, it did create memory management challenges during development.

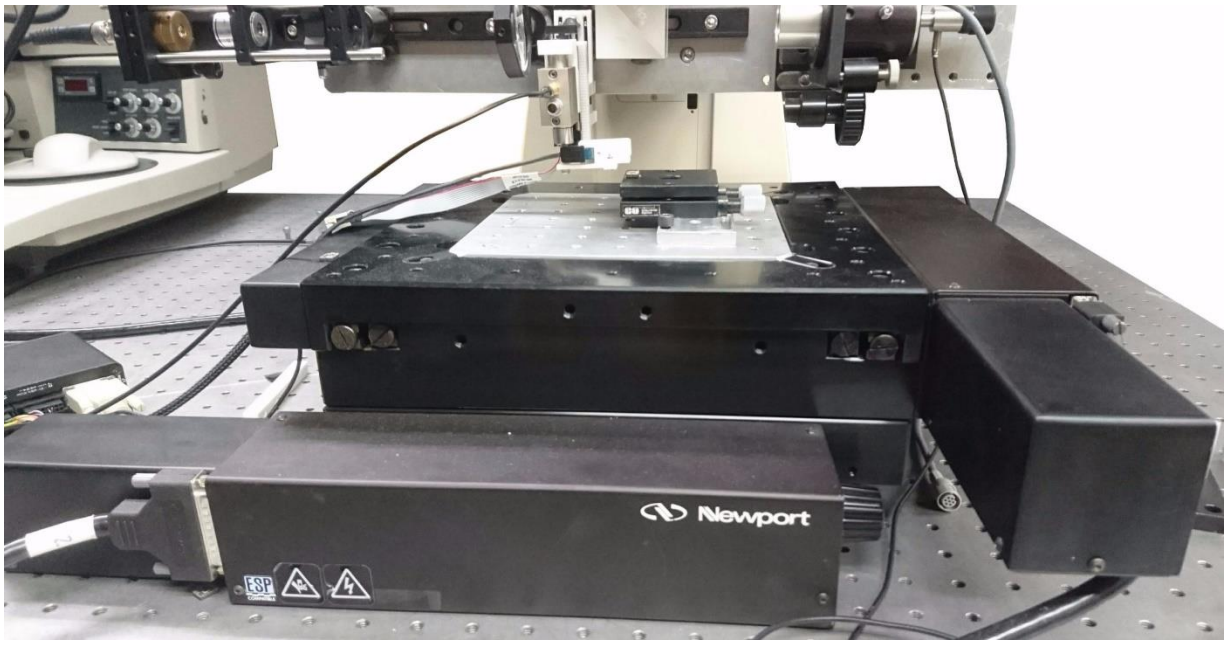

Figure 24. Newport TS-Series Linear stages used for planar positioning system
+/- 2.5µm accuracy, 0.5 um repeatability 150 mm range of motion

4.6 Vertical Positioning

The simulated and analytical results discussed in the Methodology section demonstrated that the prototype system would need very precise out of plane actuation control. However, the system also needed a practical operating range to allow for a variety of MEMS devices to be positioned for testing. Since very few actuators have both nm scale resolutions and mm scale

ranges, the vertical positioning system was split into two parts. The initial approach to the DUT is controlled by a coarse actuator while a fine actuator conducts the final probing process.

The selected coarse actuator was a National Aperture MM-3M-F.1 Linear Stage shown in Figure 25. This motorized stage provided an operating range of 25.4 mm with a resolution of 0.12 µm. However, it is important to note that while the stage has a high resolution, it has a repeatability of only 1 µm making it unsuitable for contacting the DUT.

Figure 25. Rendering of National Aperture MM-3M-F.1 Linear Stage
+/- 6 µm accuracy, 1 um repeatability, 0.12 µm resolution, 25.4 mm range of motion

The National Aperture stage was operated using a corresponding MicroMini motor controller. This controller has an intuitive serial control system which could be operated via a RS-485 connection. This meant the motor could be controlled through the MATLAB serial interface which sent motion commands to the MicroMini controller over a USB to RS-485 adapter cable.

Once the National Aperture stage had brought the force probe close to the DUT, a higher resolution actuator was needed. The team selected a Thorlabs PAZ 005 Piezo Actuator, see Figure 26, to perform this function. The PAZ 005 has a 5 nm resolution and a 20 µm range. This

makes it ideal for probing of the DUT. The PAZ 005 is able to achieve these remarkable resolutions thanks to the Piezoelectric effect.

The Piezoelectric effect is a physical phenomenon whereby some materials with crystalline structures expand or contract with changes in voltage across the material. This expansion is extremely repeatable. Piezo actuators take advantage of this property by staking disks of piezoelectric materials known as piezoceramics inside the actuator. When a voltage is applied on the system the ceramic stack expands or contracts accordingly. The relationship between this expansion and the input voltage is very precise allowing for the high actuator resolutions.

While the PAZ 005 has more than sufficient resolution for probing the DUT, the small operating range does mean that the National Aperture stage is needed to bring the probe within 20 μm before the piezo could be used. This proved to be one of the larger challenges in this project as the distance between probe location and the DUT varied with interferometer focus and magnification. Ultimately, an initial manual approach proved to be the simplest solution to this problem.

The final combination of the Newport planar stages, the National Aperture linear stage, and the Thorlabs piezo provided the probe positioning system with the three degrees of freedom needed to conduct multi point stiffness testing on the DUT.

Figure 26. Rendering of Thorlabs PAZ 005 Piezo Actuator
5 nm resolution, 20 µm range of motion

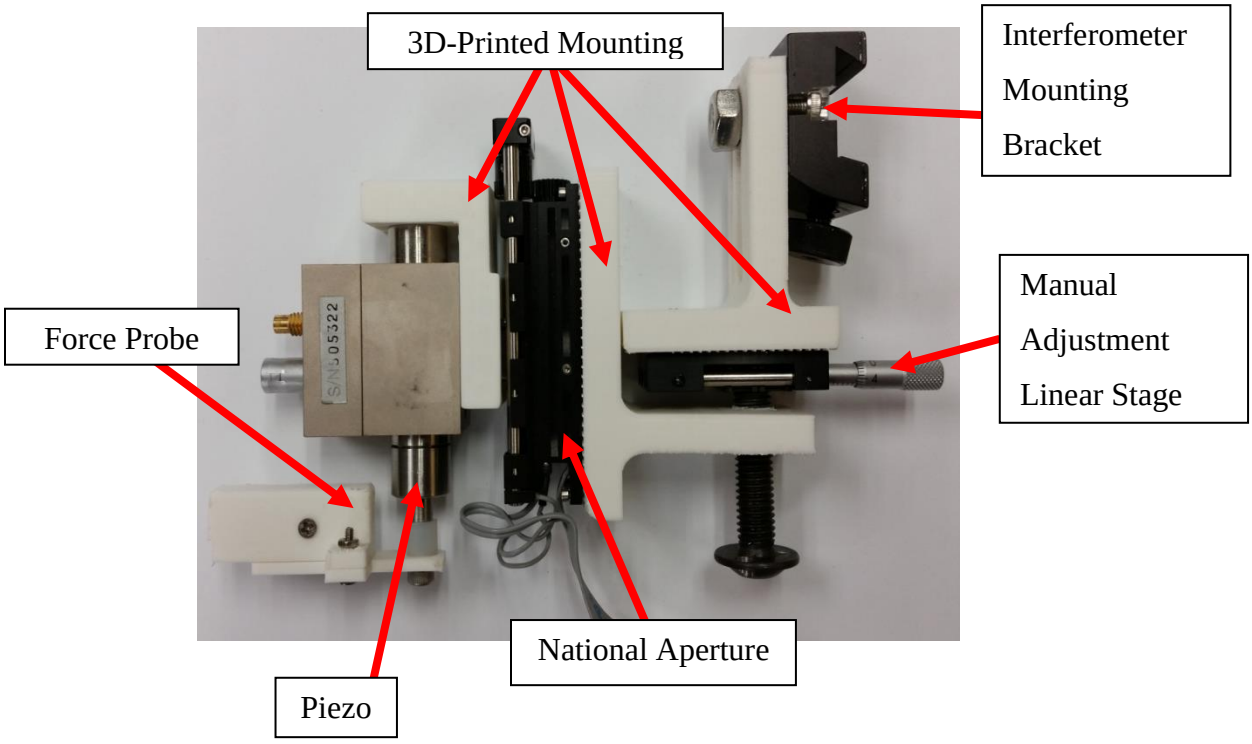

Figure 27. Mounting mechanism for vertical actuators and force probe

We chose to mount our probing mechanism on the same sliding rail that holds the lens, mirror, and beam splitter of the interferometer. This slide rail allows adjustability, and is also a convenient mounting place near the DUT. To connect the actuators and probe, we designed a series of mounting brackets. These brackets were modeled in Solidworks and 3D-printed for rapid prototyping. The brackets connect the coarse and fine actuators to the interferometer as shown in Figure 27. The system could be coarsely adjusted using vertical slots and a horizontal manual stage mounted on the first bracket.

4.7 Force Measurement System

For the application and sensing of forces, the FT-S1000-LAT probe was used. This was chosen over other probes made by FemtoTools because it satisfies the constraints of fitting under the working distance of the interferometer and obscuring the image minimally. A schematic of the force probe is shown in Figure 28. Its sensitive direction is perpendicular to the long dimension of the PCB attached to it, allowing it to take up only 12.5 mm of vertical space. The probe, seen magnified in Figure 29, operates on a principle similar to the accelerometer. As force is applied to the probe, the springs suspending the probe deflect, allowing capacitive fingers to move, whose capacitance determines the force reading.

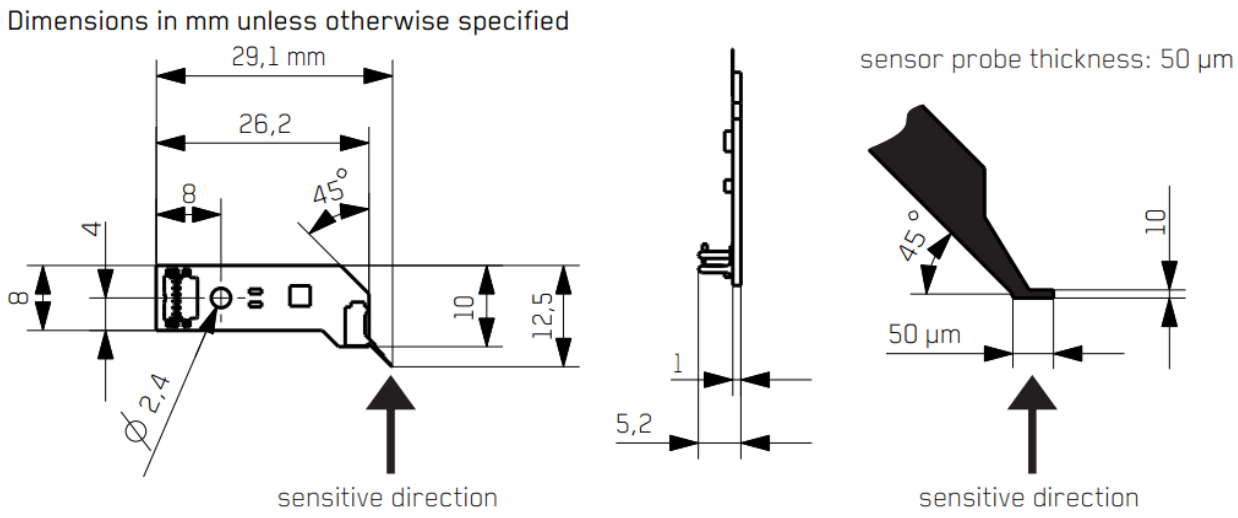

Figure 28. Schematics of the FT-S-LAT 1000 Microforce Probe

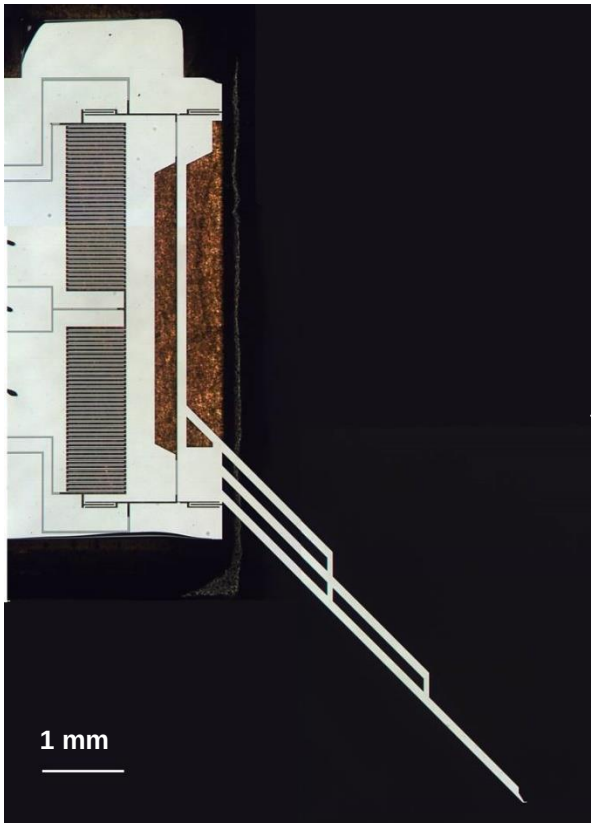

Figure 29. Microscope image of FT-S-LAT 1000 Microforce Probe

The probe has a nominal resolution of 0.5 µN at 1000 Hz sampling rate, and 0.05 µN at 10 Hz sampling rate (where 1000Hz data is averaged in 100 sample batches). We chose to sample at 1000 Hz to save time in the probing process. The probe output ranges from 0 V - 5 V with a nominal no load voltage of 2.25V. A max force of 33 µN can be applied to the probe, corresponding to 1.5 µm of proof-mass displacement according to our FEA estimation. This displacement is greater than the distance between the proof mass and the substrate, so the max force is not limited by the probe but by the accelerometer. The probe tip is a square measuring 50 µm on each side. For comparison, the proof-mass measures 309 µm on each side.

An NI USB-6009 DAQ acquired the data using MATLAB's Data Acquisition Toolbox. This DAQ has a resolution of 0.3 mV (0.15 µN), which is below the probes resolution and so is not the limiting factor. To protect the probe from dust, we designed a probe cover and machined it out of aluminum as seen in Figure 30.

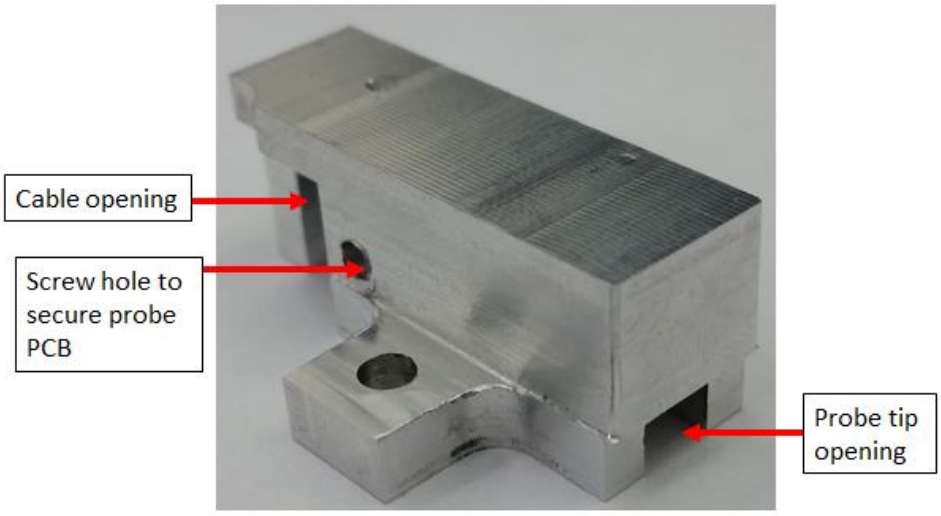

Figure 30. Force probe cover

4.7.1 Filtering of Voltage Output

Although the force probe had a nominal resolution of 0.5 μN, we measured the output signal to have 1.5 mV (0.75 μN) of noise. To take full advantage of the probe's resolution we applied an analog low pass filter to the output.

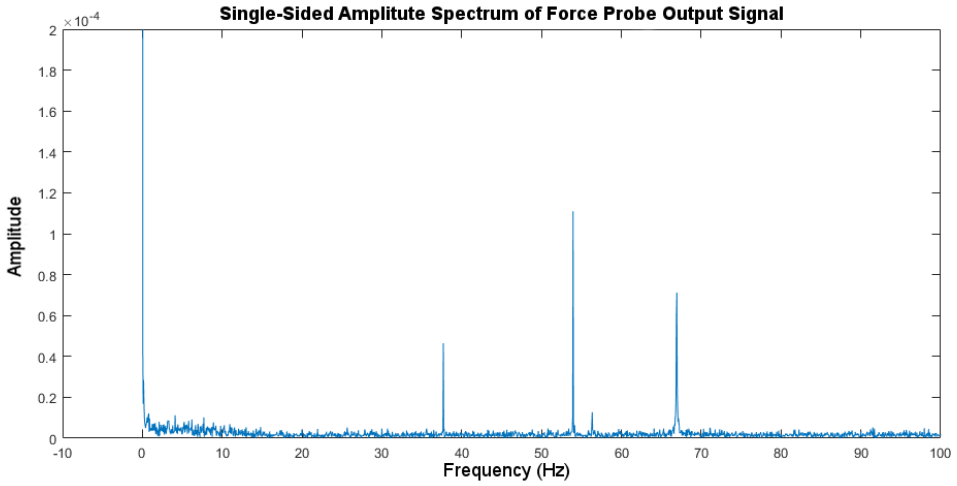

Figure 31. Result of Fast Fourier Transform on force probe output under no load

The first step in designing this filter was to consider the frequency spectrum of the noise, which we obtained using MATLAB's FFT function. The output of which can be seen in Figure 31. Small spikes can be seen at the frequencies of approximately 37 Hz, 55 Hz, 68 Hz. In other tests a fairly large but intermittent 180 Hz harmonic of noise was observed as well.

To filter the detected noise, a low-pass Butterworth filter was chosen because its response is maximally flat in the passband, and it is important for the force waveform to be undistorted if we are to draw conclusions from it. We chose an active filter using the Sallen Key topology,

shown in Figure 32, because it has no attenuation or loading, and does not require inductors which would make the circuit more expensive. The transfer function of the circuit can be seen in Equation 17.

At that time, we had not decided on an input signal to the piezo actuator, which is important information to rigorously justify the cutoff and order of the filter because it determines which frequencies the filter must pass. Taking a guess, we tried a 10 Hz 4th order filter, and when it did not reach our target, we tried increasing to 8th order. The capacitor values for 8th order were calculated in excel, see Table 6, using a table of poles and the transfer function of the Sallen Key circuit. All resistors were 100 kΩ.

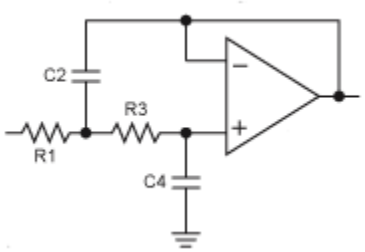

Figure 32: Sallen-Key circuit topology

$$TF = \frac{G_1 G_2}{s^2 C_2 C_4 + s2C_4 + 1} \tag{17}$$

Table 6. Capacitor values used in the 8th order force probe filtering circuit

Stage	Real pole	C4 (nF)	C2 (nF)
1	0.9808	156.1	162.3
2	0.8315	132.3	191.4
3	0.5556	88.4	286.5
4	0.1951	31.1	815.8

The cutoff frequency was experimentally found to be 10.1 Hz by adjusting a sine wave input frequency until it was attenuated by 3 dB. The MATLAB function stepinfo predicted a settling time of 0.25 seconds which was experimentally verified by applying a step input using a function generator and oscilloscope and evaluating the filter response according to the 2% criterion.

Once we agreed that the input to the piezo would be a 0.1 Hz triangle wave, the filter order and cutoff could be chosen more rigorously. To do so, a MATLAB script was developed which used real noise data to select the order and cutoff such that the standard deviation from a perfect triangle wave was minimized. This script recommended a 13 Hz cutoff 2^{nd} order filter. In hindsight, this low order makes sense, because high orders are only necessary when a large noise harmonic is very close to a signal frequency and the cutoff must be steep. However, since the team has limited time remaining and the original 10 Hz 8^{th} order filter gave a resolution of 0.559 mV (0.279 µN), which is below the probe's nominal resolution of 0.5 µN, the team continued to use it for data collection.

5.0 Results

5.1 Overview of Testing Procedures

Once the prototype was fully assembled, the design needed to be validated to demonstrate that the system was capable of reliable and accurate data collection. To do this, four separate experiments were run. The experiments are listed below. Experiments 1-3 were intended to evaluate system performance and determine physical properties. The final test was conducted on the DUT and the results were compared with the simulated and calculated expectations. In all tests, voltage readings from the force probe were collected at 1000 Hz.

1. Measuring probe output at no-load over extended time frames
2. Testing planar motion repeatability through difference images
3. Determining probe stiffness through probing of a mirror
4. Testing DUT stiffness through probing at proof mass center

5.2 Experiment 1: Measuring Probe Output at No-load

The force probe used in the prototype is an impressive piece of technology. However, over the course of system development the team observed the no-load voltage drift from the initial value of 2.25 V to higher value of 2.3 V or 2.4 V. Such drift could interfere with force calculations if not accounted for. Therefore, to better understand this behavior, the team ran a test whereby the probe was left on for 75 minutes under no-load and measured the output voltage. The result of this test can be seen in Figure 33.

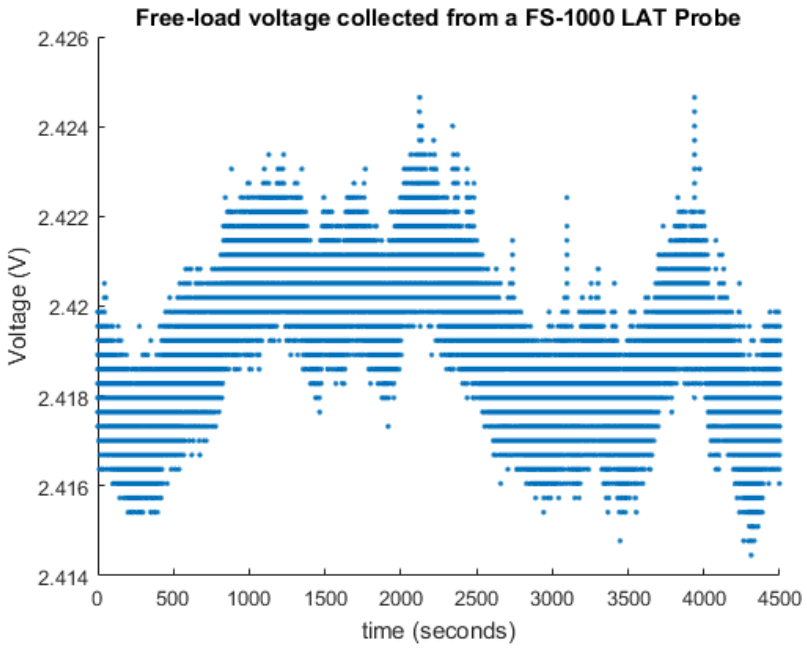

Figure 33. Force probe voltage output at no-load over a 75 minute period

As can be seen in Figure 33, the probe output drifts over long time frames. The exact cause of the drift is unclear; it could be related to temperature variations or buildup of charge in circuit capacitors. While the oscillation is concerning, further testing showed that over shorter timeframes the no-load voltage was stable enough for testing. Over timespans below 300 seconds as shown in Figure 34, where the mean sits at 2.42 V with a standard deviation of 0.559 mV (0.27 μN). This demonstrates that the probe still has sufficient resolution for testing as long as the testing can be completed in a reasonable time frame.

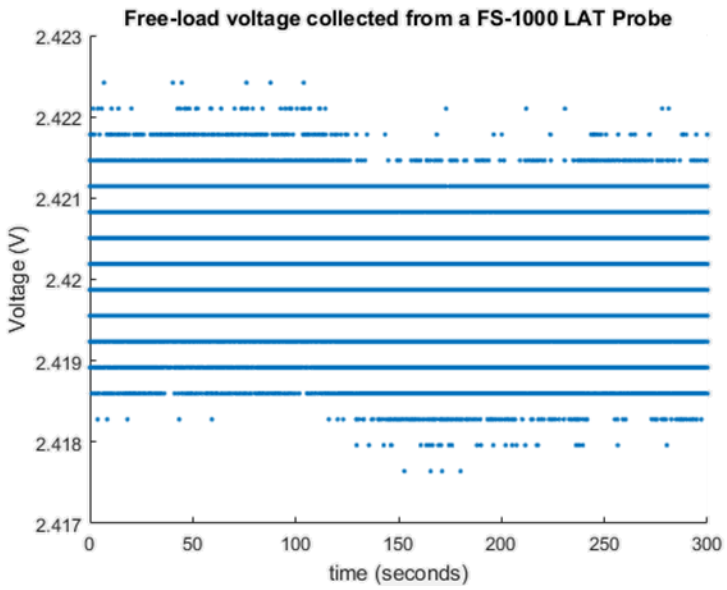

Figure 34. Force probe voltage output under no-load over 300 seconds

5.3 Experiment 2: Evaluating Planar Positioning Repeatability

Repeatability is an important characteristic for a metrology system. To evaluate the repeatability of the template matching method used for planar positioning the DUT was moved back and forth under the camera and the images at each location were compared. The process used was as follows.

1. DUT was centered under probe and image captured.
2. DUT moved so probe was positioned over upper left corner and image captured
3. DUT returned to position with probe above device center and image captured.
4. Process repeated for all corners of DUT.
5. The difference between images of the initial and final positions of the DUT was calculated to evaluate the DUT's offset from its starting position for each test.

As mentioned in step 5, the images of the DUT at each location were used to calculate a difference image between the positions. The resulting image is shown in Figure 35.

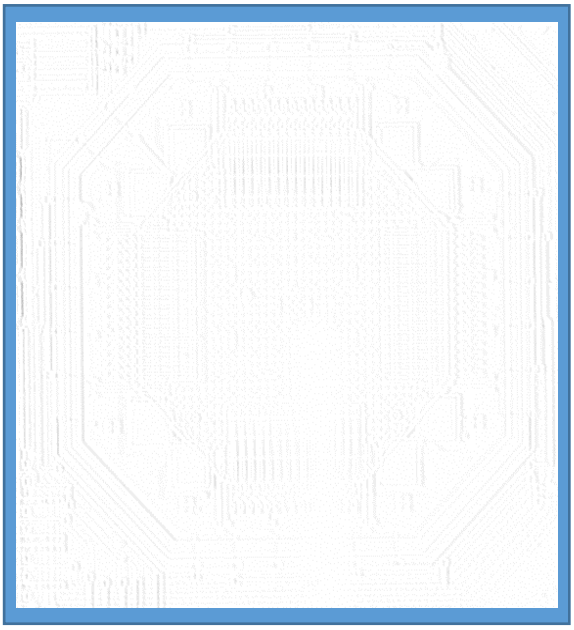

Figure 35. Difference image generated from planar positioning repeatability test.
In the test, two images are captured where the DUT is moved away and back between captures. Darkness of a pixel represents level of difference in color and therefore DUT location between images. Brightness of image demonstrates the repeatability of the planar positioning system

As evidenced by the hard to distinguish features of Figure 35, the planar positioning system is very repeatable. To quantitatively evaluate the performance, the percentage of non-white pixels were calculated for two tests. The average of the tests was 0.03%. This demonstrates that the planar positioning system was effective.

5.4 Experiment 3: Determination of Probe Stiffness from Probing a Mirror

Future usage of the metrology tool prototype may require characterization of the force probe's physical characteristics as well as proof of its repeatable output. To establish this, the probe's stiffness was tested by probing an optical mirror. A mirror provides a smooth rigid surface which can be aligned to be perpendicular to the camera using interferometry. This means that any displacement applied should be mostly loaded onto the force probe tip allowing an evaluation of probe tip stiffness. The test was conducted in the following way:

1. Probe brought within 20 μm of the mirror.
2. Piezo actuates probe into mirror to apply a preload of 31.4 μN.
3. Delay of 5 seconds occurs to allow system to settle.
4. Piezo is actuated by 0.1 Hz ramped input from function generator to reach target
5. Steps 3-4 repeated 3 times.
6. Piezo returns probe to preload.
7. Piezo retracts removing probe from device.

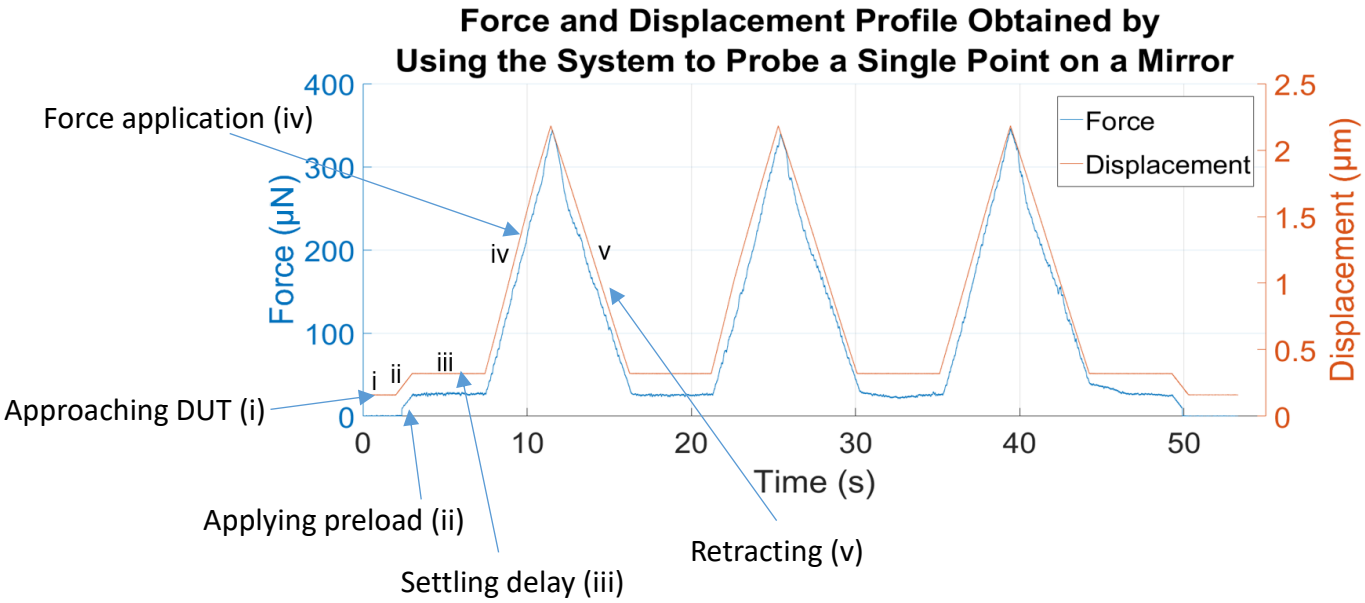

Figure 36. The force and displacement profile obtained
from using the metrology tool prototype to probe an optical mirror

The result of the experiment can be seen in Figure 36. As can be seen from the graph the prototype produced repeatable results. The test was conducted multiple times and the calculated probe stiffness from all the tests was 157 µN/µm ± 2.71%.

5.5 Experiment 4: Probing DUT at Center of Proof Mass

After confirming that our system was capable of repeated measurements, the final step was to probe the ADXL202 Accelerometer. This was done by positioning the probe above the center of the proof mass and using the function generator to actuate the probe into the proof mass. The total displacement was kept below 1.5 μm to prevent the proof mass from contacting the substrate below. The results of this test can be seen in Figure 37.

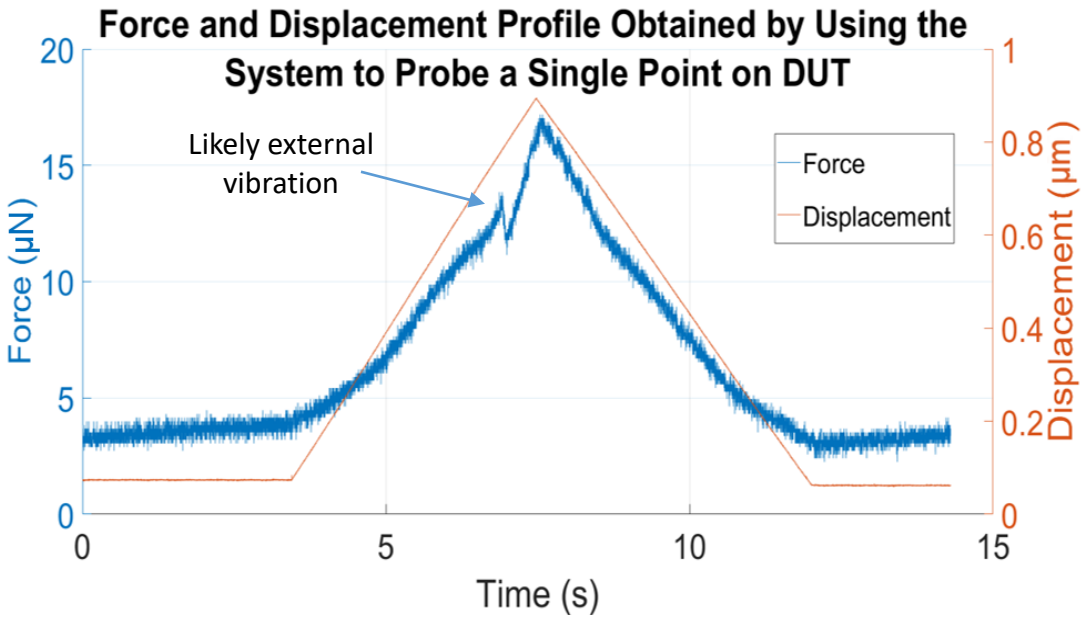

Figure 37. Force and displacement profile from probing the DUT at proof-mass center

According to the data from this test, the equivalent spring stiffness for the ADXL202 Accelerometer is 13.16 μN / μm.

5.6 Evaluation of Results from Probing DUT

In accordance with the ACES Methodology the experimental results on the DUT were compared with our analytical and simulated results. Table 7 shows all three-equivalent spring stiffness.

Table 7. Expected and observed equivalent spring stiffness values for the DUT

Method of determining stiffness	Results (μN/μm)
Analytical calculations	22
Finite element analysis	8.20
Experimental	13.16

When the expected values and observed values of spring stiffness are compared as shown in Table 7, it is clear that some discrepancy exists. Fortunately, all values are on the same order of magnitude and the experimental value falls in between the analytical value and the FEA result. This suggests that the experimental result is within reason. The large gap seen between the analytical and FEA results could be due to variations in proof mass weight. Additionally, the analytical calculations do not compensate for deformations in the proof mass itself and only evaluate forces on the folded springs. The discrepancy between the FEA and the experimental results could stem from variations in the material properties of the proof mass such as thickness and elastic modulus. Further work in analyzing the DUT using the full-field interferometer readings could help rectify this discrepancy.

6.0 Conclusions

The feasibility of a MEMS *in situ* testing system has been demonstrated through the development of a MEMS stiffness characterization tool prototype. The prototype described takes advantage of out of plane force and displacement measurements to calculate stiffness of MEMS devices. The porotype utilizes three high precision actuators and a high-resolution force probe to probe samples under an interferometer. The entire system is controlled through a custom GUI which allows for easy user operation. The reliability of the data collected using the prototype has been demonstrated on an ADXL202 Accelerometer. The results were compared with analytical calculations and finite element analysis. Results were comparable with anticipated values, but small discrepancies in the experimental data and expected values should be researched further. Such research can take advantage of the interferometer data which the prototype can provide. Using this data, the material properties of an individual die could be extracted and the performance of the MEMS evaluated. This could lead to the future development of a comprehensive wafer level testing platform.

Future work on the testing prototype should focus on scaling the system to operate on MEMS wafers. This will allow for the development of a binary testing procedure in which MEMS damaged in the manufacturing process are identified. This will allow manufactures to skip the packaging process for the damaged die. This will save revenue for the MEMS producers and potentially lead to methods for improving yield from the manufacturing process.

References

[1] "iPhone 6s - Technical Specifications - Apple," *Apple-Inc*, 2016. [Online]. Available: http://www.apple.com/iphone-6s/specs/. [Accessed: 14-Sep-2016].

[2] V. Kempe, *Inertial MEMS: Principles and Practice*. Cambridge University Press, 2011.

[3] R. Lawes, "MEMS Testing," in *MEMS Cost Analysis*, Pan Stanford Publishing, 2014, pp. 115–124.

[4] S. Nakov and T. Ivanov, "A Calibration Algorithm for Microelectromechanical Systems Accelerometers in Inertial Navigation Sensors," *arXiv:1309.5075v1 [cs.OH]* , 2013.

[5] M. Shoaib, N. H. Hamid, A. F. Malik, N. B. Zain Ali, M. Tariq-Jan, M., "A Review on Key Issues and Challenges in Devices Level MEMS Testing," *J. Sensors*, vol. 2016, pp. 1–14, 2016.

[6] L. I. J. C. Bergers, J. P. M. Hoefnagels, and M. G. D. Geers, "On-wafer time-dependent high reproducibility nano-force tensile testing," *J. Phys. D. Appl. Phys.*, vol. 47, no. 49, p. 495306, Dec. 2014.

[7] T. Kaya, B. Shiari, K. Petsch, and D. Yates, "Design of a MEMS Capacitive Comb-drive Accelerometer," in *Design of a MEMS Capacitive Comb-drive Accelerometer*, 2011.

[8] W. Kok, "Development of a wireless MEMS inertial system for health monitoring of structures," Worcester Polytechnic Institute, 2004.

[9] O. J. Woodman, "An introduction to inertial navigation," 2007.

[10] W. Wai Chi, "ANALYSIS OF THE SUSPENSION BEAM IN ACCELEROMETER FOR STIFFNESS CONSTANT AND RESONANT FREQUENCY BY USING ANALYTICAL AND NUMERICAL INVESTIGATION," Universiti Sains Malaysia, 2007.

[11] V. Steward, "Modeling of a folded spring supporting MEMS gyroscope," Worcester Polytechnic Institute, 2003.

[12] B. Koo and P. M. Ferreira, "An active MEMS probe for fine position and force measurements," *Precis. Eng.*, 2014.

[13] H. D. Espinosa, B. C. Prorok, and M. Fischer, "A methodology for determining mechanical properties of freestanding thin films and MEMS materials," *J. Mech. Phys. Solids*, no. 51, pp. 47–67, 2002.

[14] A. DiOrio, R. Morin, and E. Wilusz, "Inverse Method of Nanoindentation by Laser Interferometry," Worcester, 2008.

[15] B. A. Samuel, A. V. Desai, and M. A. Haque, “Microscale application of column theory for high resolution force and displacement sensing,” *Appl. Phys. Lett.*, 2005.

[16] “FT-G32 Force Sensing Microgripper.” [Online]. Available: http://www.femtotools.com/fileadmin/datasheets/FT-G32_Datasheet.pdf. [Accessed: 13-Sep-2016].

[17] F. Wang, R. Cheng, and X. Li, “MEMS Vertical Probe Cards With Ultra Densely Arrayed Metal Probes for Wafer-Level IC Testing,” *J. Microelectromechanical Syst.*, vol. 18, no. 4, pp. 933–941, Aug. 2009.

[18] J. Zhu, D. Zou, and S. Liu, “High Temperature Deformation of Area Array Packages by MoirC InterferometryFEM Hybrid Method.”

[19] B. D. Jensen, F. Bitsie, and M. De Boer, “Interferometric measurement for improved understanding of boundary effects in micromachined beams,” vol. 3875, no. 505, pp. 844–7465, 1999.

[20] A. Cigada, E. Leo, and M. Vanali, “MEMS GYROSCOPE: ELECTRICAL METHOD TO MEASURE THE MECHANICAL PARAMETERS AND THE QUADRATURE ERROR.”

[21] H. Yang and C. Furlong, “Analysis and characterization of high-resolution MEMS pressure sensors.”

[22] D. R. Pryputniewicz, “ACES approach to the development of micro-components.,” Worcester Polytechnic Institute, 1997.

[23] F. Beer and R. E. Johnston, *Mechanics of Materials*, 7th ed. McGraw Hill Education, 2014.

[24] ALLIED VISION TECHNOLOGIES GMBH, “AVT PIKE F-100B / F-100C Datasheet.” p. 2, 2007.

[25] S. Pertuz, D. Puig, and M. A. Garcia, “Analysis of focus measure operators for shape-from-focus,” *Pattern Recognit.*, vol. 46, no. 5, pp. 1415–1432, May 2013.

[26] Itseez, “Open Source Computer Vision Library.” 2017.

Appendix I: User Manual

In this Appendix, the setup and usage of the metrology tool is described. It is the team's hope that this manual will serve as both a usage guide and a reference for future improvements to the system. Care should be taken when handling all components and memory usage on the operating computer should be limited during operation.

System Assembly

The components needed for this system to function are as follows.

- Windows 7 32-bit computer
    - Computer must support at least one Firewire 1394b input port.
    - Three open USB ports.
    - PCI port and power supply capable of supporting a Newport ESP6000 Motion Controller Card
    - Esp6000 operation dll's installed
    - Java installed
    - MATLAB 2015b installed
    - Thorlabs APT Active-X control software
    - Vimba Viewer for AVT Cameras installed
- Thorlabs TPZ001 T-Cube Piezo Controller or equivalent
- Thorlabs PAZ 005 Piezo Actuator
- Newport ESP6000 Universal Motor Controller
- Pair of Newport TS-Series Linear Stages

- National Aperture MicroMini Motor Controller
- MM-3M-F.1 Linear Stage
- AVT Pike Digital Camera
- USB-RS485 Serial Adapter (Used for connecting to MicroMini motor controller)
- Femto Tools FT-S1000-LAT
- Probe cover and other mounting brackets.
- National Instruments USB-6009 DAQ.
- Michelson's Interferometer
- Any Laser Diode Controller
- Function Generator with external trigger

Once all of these components are collected and necessary software is installed, the valid functioning of each component should be verified independently. If each component is fully functional then the user can assemble the system. Figure 27, Figure 24, and Figure 14 provide an effective overview of the physical construction of the system.

Software Launch

To the launch the control software for this system the user will need to run MATLAB. If the user experiences memory issues while operating the software, MATLAB can be relaunched from command line using the following command on Windows 7 32-bit:

```
matlab -nodisplay -nodisplay -nosplash -nodesktop -shield maximum <all dll's loaded during matlab operation should have their paths listed here>
```

This command will launch MATLAB without its regular GUI and add sage guards for memory usage on Windows 32-bit machines. This method proved effective at allowing the software to run when memory was limited.

Once MATLAB has launch the user should navigate to the code source directory and run the MATLAB script launchGUI. This will initialize all the actuators and launch the user control GUI. Launching the GUI may take some time as the ESP6000 Universal Motor Controller is very time consuming to connect to. Once the GUI is launched actual operation of the system may begin.

User Operation

When the GUI starts successfully the user should see the GUI shown in Figure 38. The video will not be displayed until the camera is started. The appearance of buttons may very base on the exact version of Java used on the system. If the GUI fails to launch it may be because the JAR file was not compiled for the same version of Java as used by MATLAB. In this case, the user simply needs to build the new JAR file from the GUI source code and place it in the lib folder in the MATLAB path.

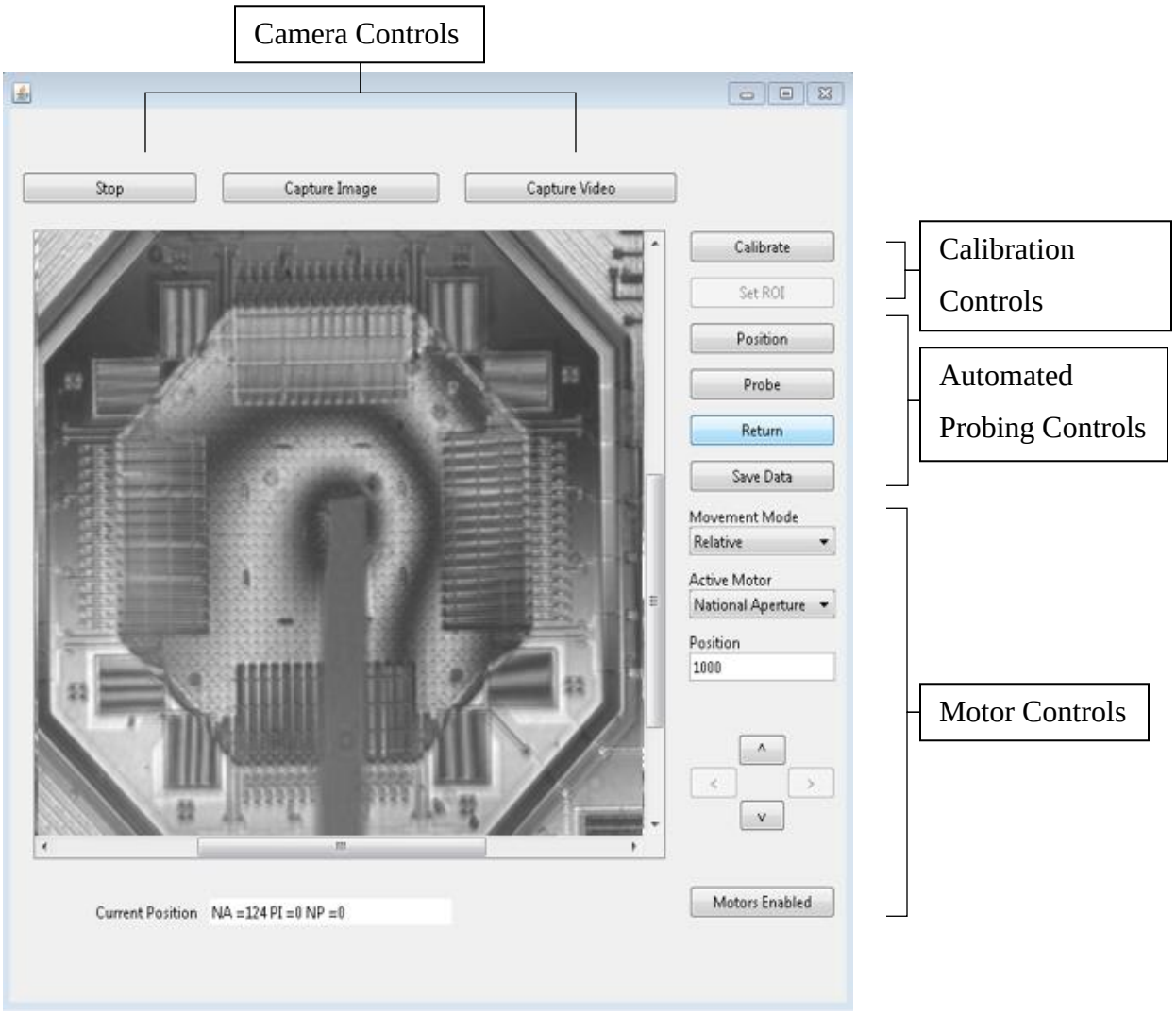

Figure 38. Java GUI with button sets labeled

The user starts the camera and captures video or images using the three buttons on the top. When a user ends the recording of video they will be prompted about whether to save the video as binary or as a.avi file. It is recommended that long videos be saved in binary format to prevent excess memory usage. The binary files can be converted back into avi files using MATLAB when the resolution, channel count, and frame rate are known.

Before the user starts the probing process they should follow the procedure below. This will ensure the system is calibrated and motors enabled in the safest order.

1. Start the camera
2. Hit the Motors Disabled button. This will change to Motors Enabled and home all motors when enabling is complete.
3. Hit calibrate and load the template image according to the prompt.
4. Jog the motors to contact the DUT.
5. Hit finish calibration after contacting the DUT and moving back a small displacement.
6. Jog the motors to the desired probing point
7. Hit probe to begin the automated probing process.
8. Save the resulting data

One of the steps listed is jogging the actuators. To do this the actuator should be selected from the drop down and then the movement mode relative or absolute selected. This should be redone after every automated probing process. The desired step size is input in the editable text box. To assign the value the user must hit enter after typing in a new value. Units for each actuator are different. The Piezo is controlled with μm values. The National Aperture stage takes

encoder tick counts as input. The Newport stages take mm as the input. The displacement of each actuator is shown in the Current Position output field at the bottom of the GUI.

Appendix II: Software Design

The code used for this project was hosted on GitHub and can be obtained by contacting Director of WPI-ME/CHSLT.

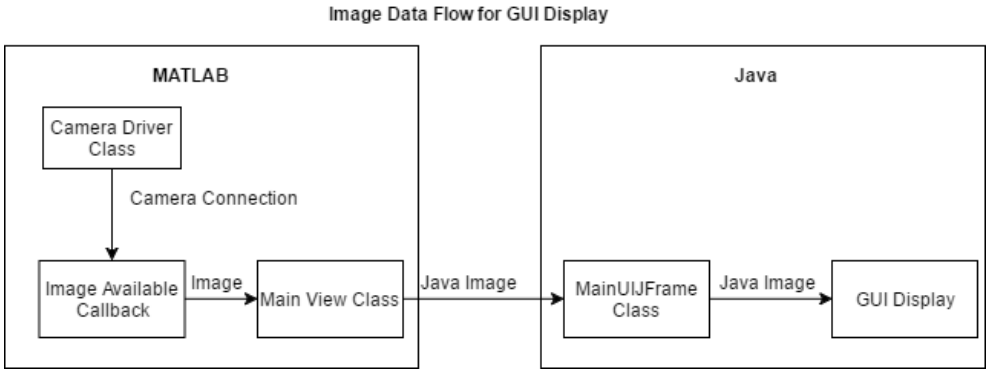

Figure 39. Flowchart of image data between MATLAB and Java.
Images captured using MATLAB's image acquisition toolbox are converted to Java Image classes before being sent to the Java GUI for display

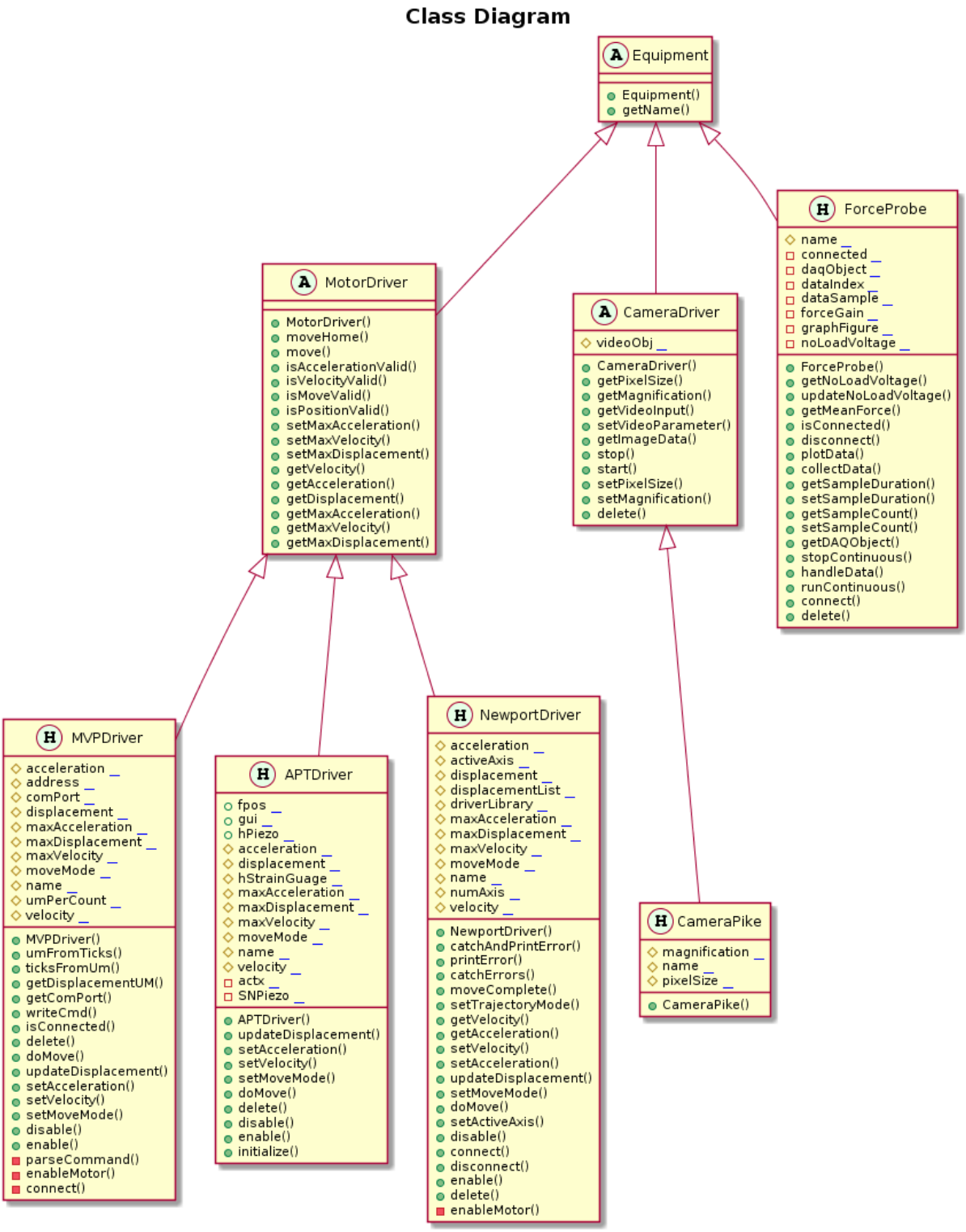

Figure 40. Part 1 of a UML class diagram for the MATLAB software. Shows the classes representing physical components of the system

Figure 41. Part 2 of a UML class diagram for the MATLAB software. Shows the primary control and display classes

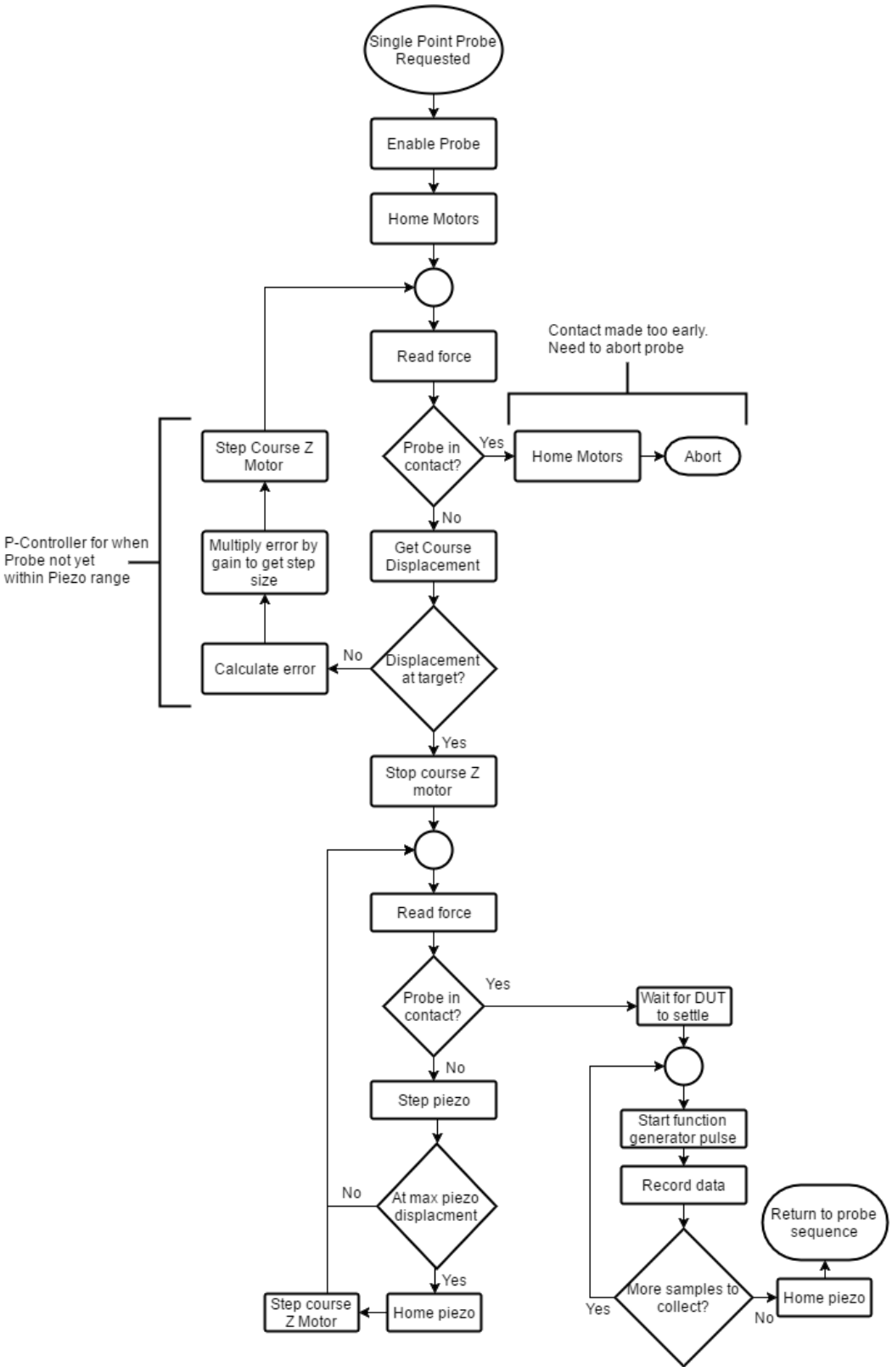

Figure 42. Automated probing process flowchart

Appendix III: Folded Spring Stiffness Calculation

```
clc; clear all; close all;
E = 0.16; % N/um2

L_BC = 6; % um
L_CD = 55.5 / 2; % um
L_AB = L_CD;
b = 2.5; % um
h = 3; % um
Ab = b * h; % um2
A_c = Ab; % um2
G = 0.69; % N/um2
I_by = h*b^3/12;
I_bx = b*h^3/12;
I_bz = 0;
I_cy = h*b^3/12;
I_cz = b*h^3/12;
c1 = 0.208;
J_c = c1*b*h^3;
J_b = c1*b*h^3;
A_b = b*h;

k_middle =  1 / ((L_AB^3-3*L_AB^2*L_CD + 3*L_AB*L_CD^2) / (3*E*I_bx) ...
    + 6*L_AB/ (5*G*A_b) + (L_BC^2*L_AB) / (G*J_b) + L_BC^3/(3*E*I_cz) ...
    + (6*L_BC) / (5*G*A_c) + (L_CD^2*L_BC) / (G*J_c) + L_CD^3/(3*E*I_bx) ...
    + 6*L_CD/(5*G*A_b));

L_CD = L_CD * 2;
k_edge = 1 / ((L_AB^3-3*L_AB^2*L_CD + 3*L_AB*L_CD^2) / (3*E*I_bx) ...
    + 6*L_AB/ (5*G*A_b) + (L_BC^2*L_AB) / (G*J_b) + L_BC^3/(3*E*I_cz) ...
    + (6*L_BC) / (5*G*A_c) + (L_CD^2*L_BC) / (G*J_c) + L_CD*0.05^3/(3*E*I_bx) ...
    + 6*L_CD/(5*G*A_b));

k_spring = 1 / (15/k_middle + 2/k_edge);

k_ef = 8*k_spring;
max_force = 0.001; % N
displacement = max_force / k_ef; %max displacement before probe breakes;
force_probe_res = 0.05; % uN
distance_resulution = force_probe_res / 1000 / 1000 / k_ef; %

k_ef
```

```
k_ef =

   2.2064e-05
```

Published with MATLAB® R2016a